nature communications

Article

https://doi.org/10.1038/s41467-024-52537-6

MFSD7C protects hemolysis-induced lung impairments by inhibiting ferroptosis

Received: 11 June 2023

Accepted: 12 September 2024

Published online: 19 September 2024

Check for updates

Huirui Wang[1,8], Xiaona You[2,8], Jingcheng Wang[1,8], Xinyi Chen[3], Yinghui Gao[1], Mengmeng Wang[1], Wenru Zhang[1], Jiaozhen Zhang[1], Yang Yu[4], Bo Han[5], Mei Qi[6], Xiaohui Liu[7] ✉, Hongxiang Lou[1] ✉ & Ting Dong[1] ✉

Hemolysis drives susceptibility to lung injury and predicts poor outcomes in diseases, such as malaria and sickle cell disease (SCD). However, the underlying pathological mechanism remains elusive. Here, we report that major facilitator superfamily domain containing 7 C (MFSD7C) protects the lung from hemolytic-induced damage by preventing ferroptosis. Mechanistically, MFSD7C deficiency in HuLEC-5A cells leads to mitochondrial dysfunction, lipid remodeling and dysregulation of ACSL4 and GPX4, thereby enhancing lipid peroxidation and promoting ferroptosis. Furthermore, systemic administration of MFSD7C mRNA-loaded nanoparticles effectively prevents lung injury in hemolytic mice, such as HbSS-Townes mice and PHZ-challenged 7 $C^{-/-}$ mice. These findings present the detailed link between hemolytic complications and ferroptosis, providing potential therapeutic targets for patients with hemolytic disorders.

Hemolysis, which describes the destruction of red blood cells in the circulation, is one of the major pathological complications of various diseases, including sickle cell disease (SCD), malaria, autoimmune diseases, and bone marrow failure[1–4]. Under homeostatic conditions, the destruction of senescent erythrocytes leads to the release of free hemoglobin, heme and iron in the intravascular environment. Excessive heme is neutralized and internalized by hemopexin and degraded in the cells to produce biliverdin, carbon monoxide, and ferrous iron by heme oxygenase (HMOX1). Extensive hemolysis during hemolytic diseases overwhelms the heme and iron homeostasis and saturates their scavenger molecules[5]. Failure to regulate heme and iron leads to oxidative stress and inflammation, resulting in irreversible cellular and tissue damage or cell death[5]. Specifically, uncontrolled iron release to the circulation during hemolysis triggers ferroptosis in normal and non-nucleated cells such as platelets[6].

Ferroptosis is an iron-dependent form of cell death induced by extensive iron accumulation and lipid peroxidation[7]. While inserting polyunsaturated fatty acids (PUFAs) enhances membrane fluidity, excess oxidation of PUFAs could lead to cell oxidative crisis[8]. Ferroptosis has been suggested to participate in pulmonary diseases due to abnormal iron or redox homeostasis in patients with lung diseases. For example, the mouse with acute lung injury was characterized by ferroptotic physiological features, including iron overload, glutathione (GSH) consumption and malondialdehyde (MDA) accumulation, and downregulation of SLC7A11 and GPX4 expression levels in the lung tissues[9]. Similarly, in chronic destructive pulmonary disease setting, bronchial epithelial cells exposed to cigarette smoke has demonstrated endothelium reticulum stress and mitochondrial dysfunction, accompanied by insufficient levels of GPX4 and GSH, resulting in iron accumulation and ferroptosis[10]. In addition, ferroptosis also has a pathological role in pulmonary fibrosis, as evidenced by the increased

[1]Department of Natural Products Chemistry, Key Lab of Chemical Biology of the Ministry of Education, Shandong University, Jinan, China. [2]Institute of Immunopharmaceutical Sciences, School of Pharmaceutical Sciences, Shandong University, Jinan, China. [3]Division of Infection and Immunity, University College London, London, USA. [4]Advanced Medical Research Institute, Cheeloo College of Medicine, Shandong University, Jinan, China. [5]Department of Pathology, Shandong University School of Basic Medical Sciences, Jinan, China. [6]Department of Pathology, Shandong University Qilu hospital, Jinan, China. [7]State Key Laboratory of Bioactive Substance and Function of Natural Medicines, Institute of Materia Medica, Chinese Academy of Medical Sciences and Peking Union Medical College, Beijing, China. [8]These authors contributed equally: Huirui Wang, Xiaona You, Jingcheng Wang.
✉e-mail: xiaohuiliu@imm.ac.cn; louhongxiang@sdu.edu.cn; dongting2016@gmail.com

lipid peroxidation and ROS production, leading to differentiation and activation of fibroblast in response to erastin[11]. However, detailed mechanisms of how ferroptosis induces lung damage require more focused research.

Major facilitator superfamily domain containing 7 C (MFSD7C), also referred as feline leukemia virus subgroup C receptor 2 (FLVCR2) and SLC49A2, was initially identified to mediate heme-iron trafficking in macrophage[12]. However, further studies did not observe a change in heme levels in neither MFSD7C overexpressed nor knockout mice[13,14]. A recent study reported that MFSD7C is a choline transporter at the blood–brain barrier, and expression of MFSD7C in cells can significantly increase choline uptake[15]. Our previous study showed that MFSD7C regulates mitochondrial energy metabolism by switching ATP synthesis to thermogenesis in response to heme levels in macrophages[14]. Nevertheless, the role of MFSD7C in ferroptosis and hemolytic-associated lung damage has never been investigated.

In the present work, we investigated the role and the underlying mechanism of MFSD7C in lung damage in a hemolytic mouse model. We found that MFSD7C protected the pulmonary cells from ferroptosis by stabilizing mitochondrial function and regulating the expression of GPX4 and ACSL4 to prevent lipid peroxidation. MFSD7C knockout exacerbated pulmonary inflammation and lung fibrosis by encouraging ferroptosis in the lung. The administration of MFSD7C mRNA-loaded nanoparticles effectively improved lung damage in hemolytic mice model.

Results

Hemolytic-related lung damage was observed in SCD mice

SCD, characterized by severe hemolytic anemia, links to multiple anemia complications, including lung injuries[16]. However, the exact pathological mechanism remains unknown. To characterize the hemolytic-related lung damage, we employed HbSS-Townes mice as the SCD mice model in which the murine α and β globins were replaced by human α and βS globins. Meanwhile, HbAA-Townes mice were used as the control mice (Fig. S1a). Similar to patients with SCD, the bilirubin level as well as the serum heme level were significantly increased in 12-month old HbSS-Townes mice compared to the control mice (Fig. S1b and Fig. 1a). Meanwhile, HbSS-Townes mice displayed decreased hemopexin resulting in increased free heme levels (Fig. 1a). Consistent with the excess free heme in serum, severe pulmonary inflammation was seen in these HbSS-Townes mice, as indicated by increased immune cell infiltration in lung tissues (Fig. 1b) and elevated

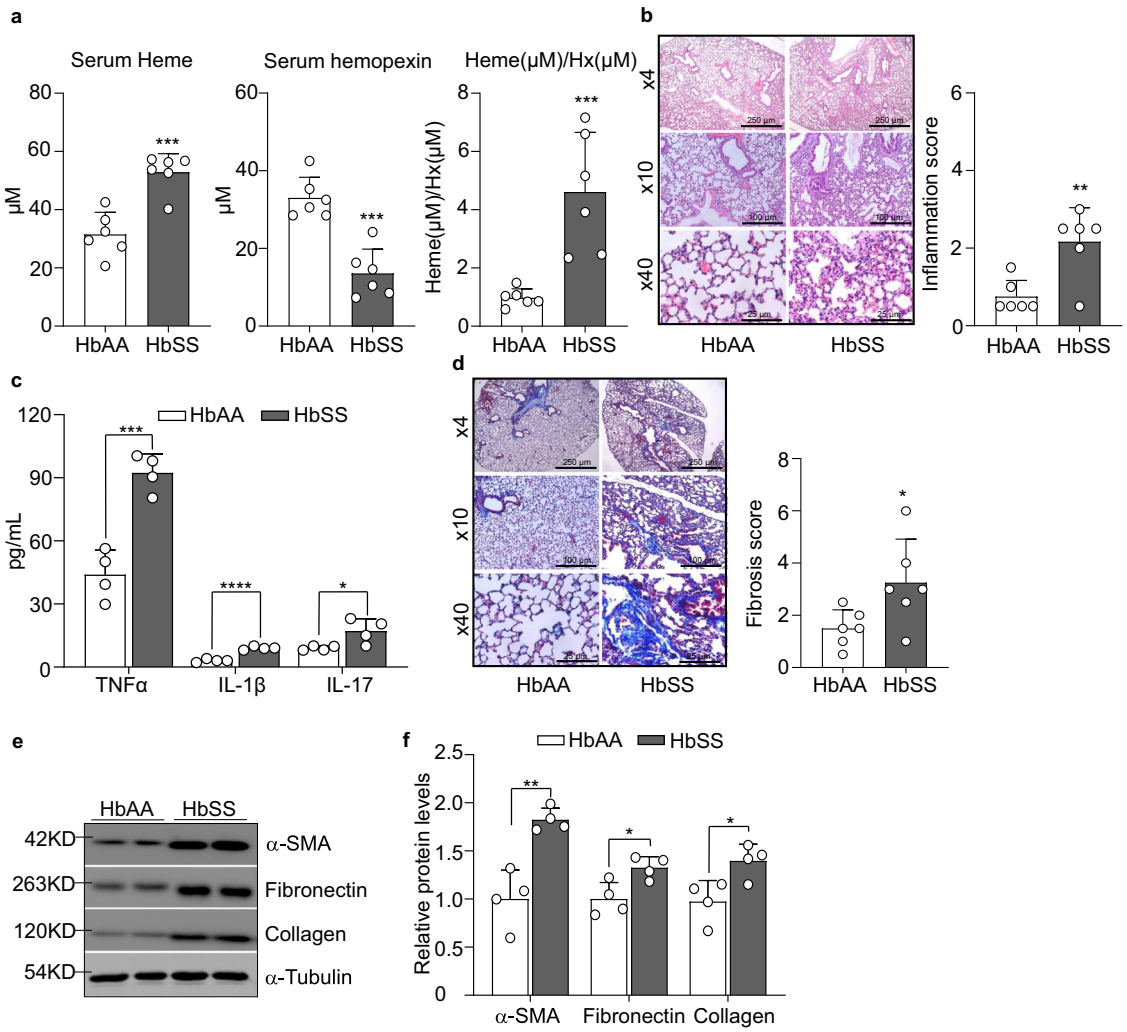

Fig. 1 | Hemolytic-related lung damage was observed in SCD mice. a–f HbAA- and HbSS-Townes mice were analyzed at 12 months. **a** Serum heme and hemopexin (Hx) levels were measured by ELISA. n = 6. **b** Representative micrographs on lung sections (H&E, x4, x10, x40) and inflammation score were shown. $n = 6$. **c** Cytokines levels, including TNFα, IL-1β, and IL-17 in murine BALF were measured by ELISA. $n = 4$. **d** Representative micrographs on lung sections (Masson's trichrome, x4, x10, x40) and fibrosis score were shown. $n = 6$. Representative western blot (**e**) and quantitative analysis (**f**) of α-SMA, Fibronectin, and Collagen expression in lung tissue. Four biological replicates were performed for each sample. Data are presented as mean + standard deviation (SD). $^{*}p < 0.05$; $^{**}p < 0.01$; $^{***}p < 0.001$; $^{****}p < 0.0001$.

proinflammatory cytokines production (Fig. 1c). Furthermore, HbSS-Townes mice were also characterized by aggravated pulmonary fibrosis, as evidenced by the provoked collagen deposition (Fig. 1d), and increased protein and mRNA expression of fibrosis markers, including alpha-smooth muscle actin (α-SMA), fibronectin and collagen (Fig. 1e, f, Fig. S1c, d). However, the lung injury phenotype was not seen in 3-month-old HbSS-Townes mice (Fig. S1e, f), suggesting that lung inflammation and fibrosis was closely associated with advancing age. Together, we confirmed that profound lung damage was observed in mice with SCD due to severe hemolysis.

The MFSD7C expression level was downregulated in hemolytic lung

As MFSD7C possess a role in heme regulation, we aimed to explore the pathological role of MFSD7C in hemolytic complications. To investigate whether MFSD7C is involved in hemolytic-related damage, we first analyzed MFSD7C expression in different tissues of HbAA-Townes mice. Significantly higher levels of MFSD7C mRNA and protein content were seen in the murine lung compared to other tissues, which suggests a potential role of MFSD7C in the lung (Fig. 2a and Fig. S2a, b). Then, we compared the MFSD7C expression between 12-month-old HbSS-Townes and HbAA-Townes mice. Interestingly, reduced expression of MFSD7C was observed in the lung tissue from HbSS-Townes mice, along with an increased level of HMOX-1, an essential enzyme in heme metabolism (Fig. 2b). Not surprisingly, the expression of MFSD7C in 3-month old HbSS mice is comparable with that in HbAA mice (Fig. S2c, d). The decline of MFSD7C and upregulation of HMOX-1 were also observed by qPCR and immunohistochemical staining in HbSS-Townes mice's lungs (Fig. 2c, d and Fig. S2e). Moreover, the MFSD7C and HMOX-1 expression was confirmed in phenylhydrazine (PHZ)-induced hemolytic mice's lung and heme-treated human pulmonary endothelial cell line (HuLEC-5A) (Fig. S2f, g). To identify the cell types in which MFSD7C expression is reduced in HbSS mice, epithelial (Fig. S2h), endothelial cells (Fig. S2i) and alveolar macrophages (AMs) in the lung were enriched. Notably, reduced expression of MFSD7C was observed in AMs and endothelial cells, but not in epithelial cells of HbSS-Townes mice (Fig. 2e). Colocalization of MFSD7C and macrophage or endothelial cell markers confirmed the expression of MFSD7C on these cell types (Fig. 2f). These data suggest that expression of MFSD7C in AMs and endothelial cells might have a protective role in hemolytic-related lung damage.

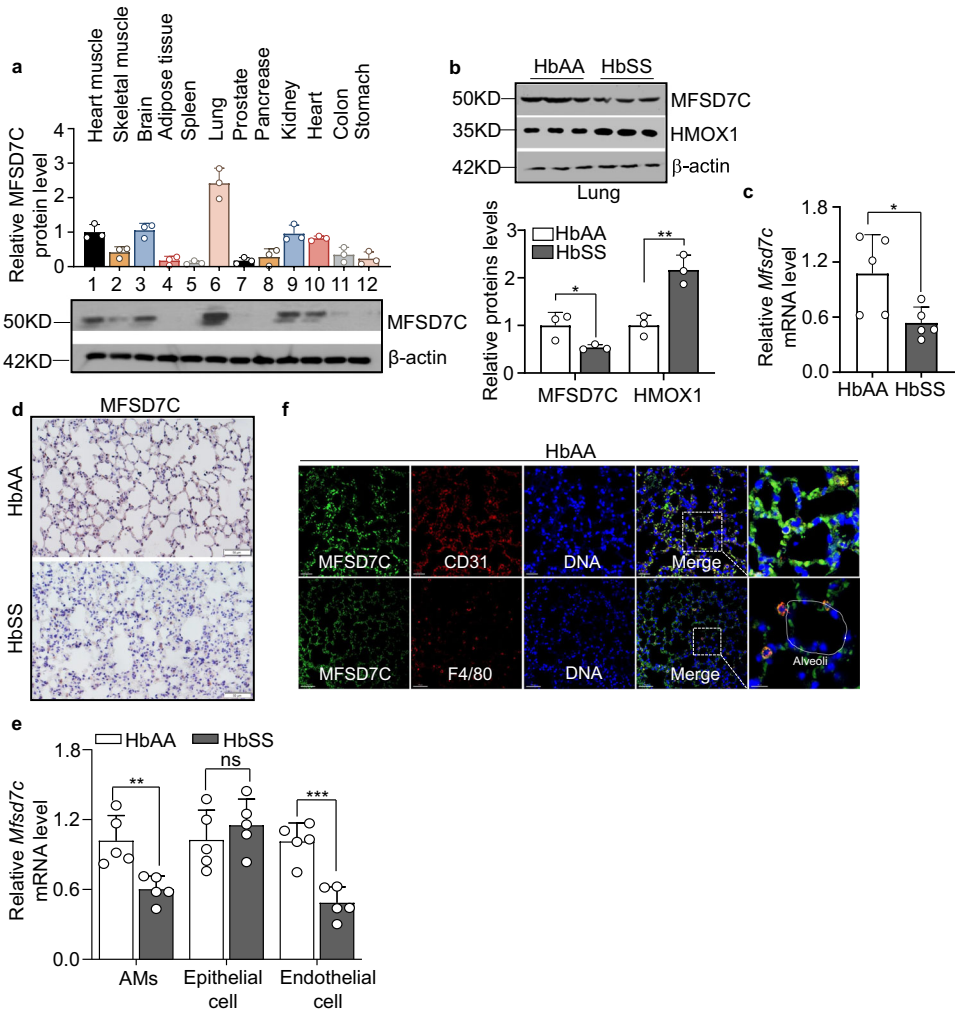

Fig. 2 | The MFSD7C expression level was downregulated in alveolar macrophages and endothelial cells of hemolytic lung. a Relative MFSD7C protein levels in various tissues of 8 weeks old HbAA-Townes mice. $n = 3$. **b**–**d** 12-month old HbAA- and HbSS-Townes mice were analyzed. **b** Expression levels of MFSD7C and HMOX1 in lung tissues were analyzed using western blot. Three biological replicates were performed for each sample. **c** Changes in the mRNA expression of MFSD7C of lung tissues from hemolytic mouse model were evaluated by RT-qPCR. $n = 5$. **d** IHC staining of MFSD7C in lung samples. **e** Relative MFSD7C mRNA level in AMs, epithelial cells, and endothelial cells isolated from lung tissues. $n = 5$. **f** Representative immunofluorescence images of lung tissues in HbAA mice (MFSD7C in green, CD31 and F4/80 in red, and nuclei in blue, photomicrograph bar = 5 μm). Data are presented as mean + standard deviation (SD). $^{*}p < 0.05$; $^{**}p < 0.01$; $^{***}p < 0.001$.

https://doi.org/10.1038/s41467-024-52537-6

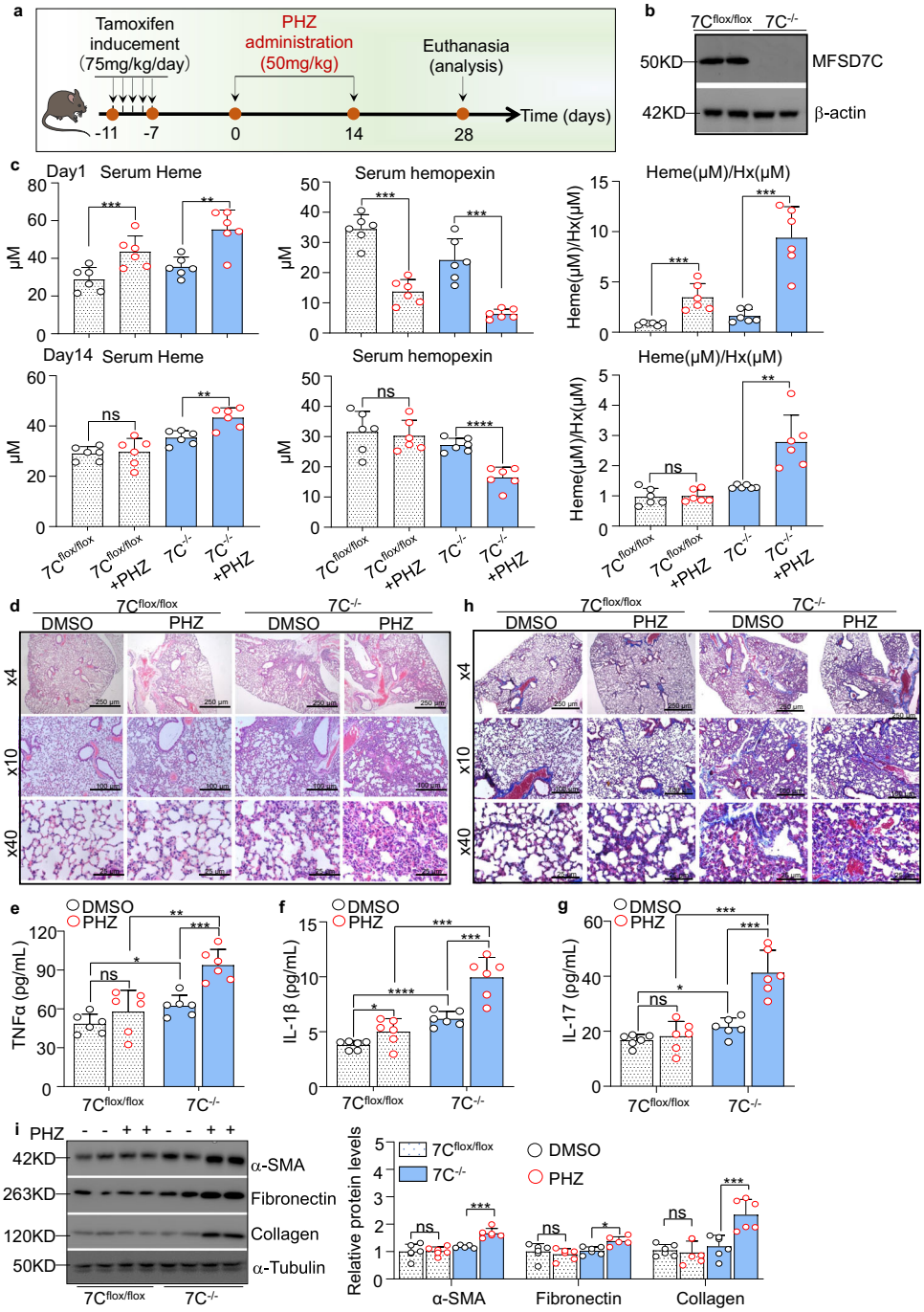

Fig. 3 | Deficiency of MFSD7C aggravates pulmonary damage in PHZ-induced hemolytic diseases. a Experimental scheme of tamoxifen inducement and PHZ administration. **b** Representative western blot of MFSD7C expression in lung tissues from $7C^{flox/flox}$ and $7C^{-/-}$ mice 7 days after Tamoxifen treatment. Four biological replicates were performed for each sample. **c** Serum heme and hemopexin (Hx) levels were measured at day 1 and day 14 (just before 2nd PHZ administration) by ELISA. $n = 6$. **d**–**i** $7C^{flox/flox}$ and $7C^{-/-}$ mice treated with DMSO or PHZ were analyzed at day 28. **d** Representative lung H&E staining sections (x4, x10, x40). TNFα (**e**), IL-1β (**f**), and IL-17 (**g**) levels in BALF were measured by ELISA. $n = 6$. **h** Representative lung Masson's trichrome staining (x4, x10, x40). **i** Expression levels of α-SMA, Fibronectin, and Collagen expression in lung tissues were analyzed using western blot. $n = 6$. Data are presented as mean + standard deviation (SD). $^{*}p < 0.05$; $^{**}p < 0.01$; $^{***}p < 0.001$; $^{****}p < 0.0001$.

Deficiency of MFSD7C aggravates lung damage in PHZ-induced hemolytic mouse model

To assess the protective role of MFSD7C in hemolytic-related lung damage, we generated tamoxifen-induced MFSD7C knockout ($7C^{-/-}$) mice (Fig. S3a). For the hemolytic mouse model, the mice were injected with tamoxifen inducement for five days, and 7 days later, the mice were challenged with PHZ (which induces intravascular hemolysis by lipid peroxidation of erythrocyte membranes[17]) on day 0 and 14, finally sacrificed on day 28 for analysis (Fig. 3a). MFSD7C knockout was confirmed with western blot and immunohistochemical analysis (Fig. 3b and Fig. S3b). Similar to HbSS mice, both $7C^{-/-}$ and $7C^{flox/flox}$ mice displayed increased serum heme levels and depleted hemopexin after one day upon 1st PHZ administration due to hemolysis. However, after 14 days, the increased serum heme and depleted hemopexin levels were recovered in $7C^{flox/flox}$ mice but not in $7C^{-/-}$ mice (Fig. 3c). In line with the free heme level in serum, the expression of MFSD7C in lung

tissues was decreased at day 1 and restored at day 14 in $7C^{flox/flox}$ mice (Fig. S3c), suggesting that MFSD7C downregulation could occur due to excess serum heme. Consistent with the sustained hemolysis, 28 days after 1st PHZ treatment, the $7C^{-/-}$ mice displayed prolonged pulmonary inflammation, as evidenced by intensive immune cell infiltration, increased proinflammatory cytokine production and total Bronchoalveolar lavage fluid (BALF) cells (Fig. 3d–g and Fig. S3d, e). Meanwhile, aggravated collagen deposition, amplified fibrosis markers, and increased lung weight indicated severe fibrosis in the lung from $7C^{-/-}$ mice treated with PHZ (Fig. 3h, i and Fig. S3f–h). On the other hand, only mild inflammation and fibrosis were observed in $7C^{flox/flox}$ mice with PHZ challenge. Together, these observations suggest that MFSD7C possess a protective role against PHZ-induced lung damage.

MFSD7C deficiency leads to mitochondrial dysfunction and lipid remodeling

To identify the role of MFSD7C, we performed RNA sequencing (RNA-Seq) analysis in MFSD7C-KO HuLEC-5A cells versus control. Dysregulation in pathways related to brain disorders in the MFSD7C knockout cells was highlighted in pathway analysis (Fig. 4a and Fig. S4a), which is consistent with its role in early brain development found in another study[13]. Meanwhile, dysregulation in thermogenesis, oxidative phosphorylation, and glutathione metabolism, emphasized the non-negligible role of MFSD7C in metabolic regulation and energy production (Fig. 4a and Fig. S4a). To validate the function of MFSD7C on oxidative phosphorylation, we analysed the rate of oxygen consumption rate (OCR) by seahorse analysis. We noticed that OCR was significantly increased in AMs and endothelial cells from PHZ-treated $7C^{-/-}$ mice, along with reduced ATP production (Fig. 4b, c and Fig. S4b–i). PHZ treatment further boosted ROS production and lipid ROS accumulation in AMs (Fig. 4d, e and Fig. S4j, k). In line with the reduced ATP production, 7C-KO HuLEC-5A cells demonstrated a loss in mitochondrial membrane potential, which indicates a disruption of the TCA cycle in mitochondria (Fig. 4f, g). Interestingly, despite the defected TCA cycle is defected, fatty acid uptake, but not glucose, significantly elevated in 7C-KO HuLEC-5A cells, suggesting that an alternative pathway was adapted to metabolize lipids in the cells (Fig. 4h and Fig. S4l). While aberrant metabolism was observed in the MFSD7C-deficient cells, re-introduction of the gene rescued the cell from impaired ATP production and mitochondrial functions, and re-balance the lipid uptake by the cells (Fig. 4f–h and Fig. S4j–l). In view of the altered metabolic profile in MFSD7C knockout cells, we hypothesized that MFSD7C is involved in lipid metabolism. The quantification of the abundance of fatty acid using high performance liquid chromatography-mass spectrometry highlighted the increased medium- and long-chain fatty acid in the level of triglycerides (TG), phosphatidyl-ethanolamines (PE), alkenyl-phosphatidylethanolamine PE(P) and alkyl-phosphatidylethanolamine PE(O), which consist of PUFAs, remarkably increased in MFSD7C knockout AMs compared to the control (Fig. 4i, j and Fig. S4m–p, Tables S2–S4). Importantly, the upregulation of free unesterified arachidonic acid was further validated in MFSD7C knockout HuLEC-5a cells and lung tissues of $7C^{-/-}$ mice and HbSS mice (Fig. S4q–s). Notably, aggravated lipid oxidation was observed in 7C-KO HuLEC-5A cells treated with exogenous heme or RAS-selective lethal 3 (RSL3), a ferroptosis inducer (Fig. S4t, u). Together, these results support the role of MFSD7C in regulating mitochondria function and lipid peroxidation.

MFSD7C deficiency increased lipid flux by inducing CD36 and FABP4 expression

During lipid metabolism, fatty acids are transported into the cell via the scavenger receptor CD36 and fatty acid transporters proteins SLC27 family. The fatty acids then bind to fatty acid binding protein 4 (FABP4) and are broken down by acyl-CoA oxidase 1 (ACOX1), followed by further translocation to mitochondria through carnitine palmitoyltransferase 1/2 (CPT1/2) to supply the TCA cycle and energy production (Fig. 5a)[18]. We observed a significant increased expression in the gene encoding proteins related to cellular and mitochondrial translocation of fatty acid, including *CD36*, *SLC27A* family members, and *FABP4* in 7C-KO HuLEC-5A cells (Fig. 5b). On the other hand, the gene expression of *CPT1A* was decreased upon MFSD7C depletion (Fig. 5b). The dysregulated gene expression was confirmed by RT-qPCR in AMs from the lung of $7C^{-/-}$ mice (Fig. 5c). However, the expression of FASN in $7C^{-/-}$ AMs was comparable with that in control. In line with the upregulated mRNA levels, increased CD36 and FABP4 proteins was observed in AMs from HBSS-Townes and $7C^{-/-}$ mice (Figs. 5d and S5a). Hence, we suspected that increased lipid influx through CD36 and FABP4, but not lipid synthesis, promotes lipid accumulation in MFSD7C deficient cells. To investigate the role of CD36 and FABP4 in MFSD7C deficiency-induced lipid remodeling, we employed CD36 KO and FABP4 KO in HuLEC-5A cells. The generation of CD36 and FABP4 KO cells with/without MFSD7C KO were confirmed by western blotting (Fig. 5e). As the result, the elevated lipid uptake and lipid oxidation in MFSD7C KO cells were reverted by CD36 KO and FABP4 KO (Fig. 5f–i and Fig. S5b–e). Fatty acids are further broken down via β-oxidation to supply mitochondrial respiration. In agreement with reduced lipid uptake, the upregulated rate of OCR in MFSD7C KO cells was suppressed by CD36 KO, characterized by a reduction in basal and maximum respiration, proton leak (Fig. 5j–m). A similar inhibitory effect on the rate of OCR was seen in MFSD7C KO cells upon FABP4 knockout (Fig. S5f–i). Taken together, the loss of MFSD7C enhanced lipid influx by promoting CD36 and FABP4 expression.

MFSD7C deficiency enhanced ferroptosis contributes to the lung inflammation and fibrosis

Since extensive lipid peroxidation was observed in MFSD7C knockout cells under hemolytic conditions, we next focused on the potential role of MFSD7C in ferroptosis. Interestingly, the RNA-seq data showed that ferroptosis-related genes were dysregulated in 7C-KO HuLEC-5A cells versus control. The deficiency of *MFSD7C* was accompanied by upregulation of *HOMX1*, ferroptotic genes, including acyl-CoA synthetase long chain family member 4 (*ACSL4*), transferrin receptor 2 (*TFR2*); proinflammatory cytokine, including Interleukin (IL)-18, and tumor necrosis factor (TNF); and collagen-related genes, including *COL4A3*, *COL8A1*, and *COL11A1* (Fig. 6a). On the other hand, the downregulation of glutathione peroxidase 2(*GPX2*) and *GPX4*, the antioxidant defense enzyme which repairs lipid oxidative damage and inhibits ferroptosis, were decreased in 7C knockout cells. The upregulated HMOX1 and ACSL4, as well as the downregulated GPX4 expression, in the AMs from HBSS-Townes mice and $7C^{-/-}$ mice treated with PHZ were confirmed by qPCR analysis and western blot analysis (Fig. 6b and Fig. S6a–d, 6f). In addition, same differential gene expression pattern was also seen in pulmonary endothelial cells isolated from both HBSS-Townes mice and $7C^{-/-}$ mice following PHZ treatment (Fig. 6b and Fig. S6a, c, e). Meanwhile, severe oxidative stress was observed in AMs from HbSS-Townes and 7C knockout HuLEC-5A cells, as indicated by the elevated Malondialdehyde (MDA), the main products of PUFAs peroxidation, and reduced antioxidant GSH level (Fig. 6c and Fig. S6g). Together, the downregulation of MFSD7C under hemolytic conditions dysregulated ferroptosis-related genes *GPX4* and *ACSL4*, and provoked oxidative stress in the cells, suggesting the important role of MFSD7C in ferroptosis.

As expected, upon the administration of RSL3, AMs from HbSS-Townes and $7C^{-/-}$ mice demonstrated significantly lower cell survival rate compared to the controls (Fig. 6d). In addition, the RSL3-induced cell death was efficiently inhibited by ferroptosis inhibitor ferrostatin-1 (Fer-1), but not other cell death inhibitors, confirming that the increased cell death in hemolytic AMs was mediated by ferroptosis (Fig. S6h). Notably, knockouts of CD36 and FABP4 rescued the cells

https://doi.org/10.1038/s41467-024-52537-6

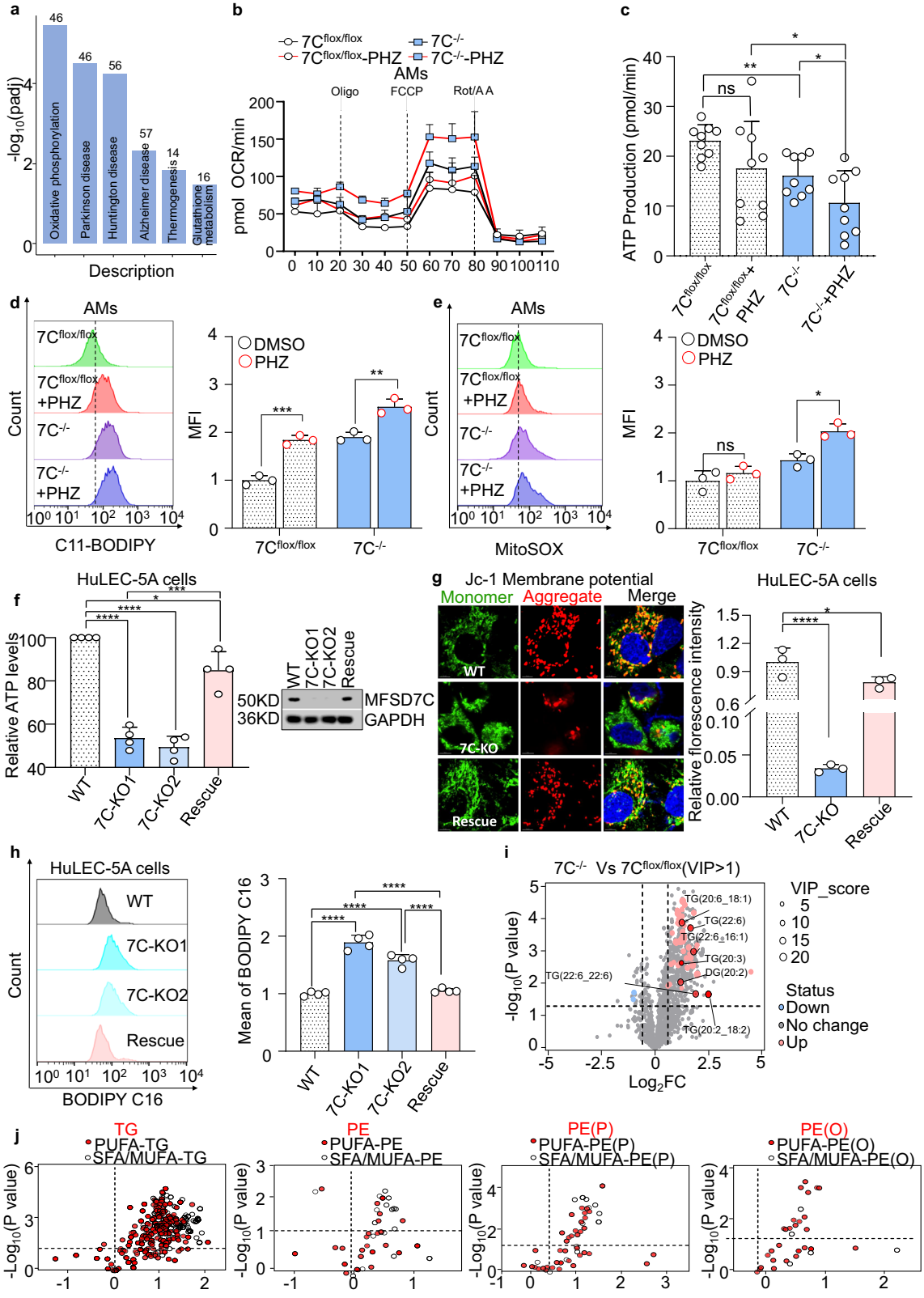

from undergoing ferroptosis, suggesting that increased lipid influx contributes to lipid peroxidation caused by MFSD7C deficiency (Fig. S6i, j). Similarly, the inhibition of CD36 with sulfosuccinimidyl oleate also protected the cells from ferroptosis, confirming the essential role of MFSD7C in lipid peroxidation to protect cells from ferroptosis (Fig. 6e). Moreover, RSL3-treated 7C-KO HuLEC-5A cells displayed altered mitochondria morphology, which is characterized by elongated structure and reduced cristae density, suggesting that the function of mitochondria is compromised due to MFSD7C deficiency under ferroptotic conditions (Fig. 6f).

Furthermore, increased production of proinflammatory cytokines was seen in hemolytic alveolar macrophages, which is inhibitable by Fer-1 (Fig. 6g). Meanwhile, we employed the exaggerated extracellular matrix deposition assay to investigate the effect of MFSD7C depletion

https://doi.org/10.1038/s41467-024-52537-6

Fig. 4 | MFSD7C regulates lipid remodeling by causing mitochondria dysfunction. a KEGG pathway analysis of differentially expressed genes (DEGs) (log_2(fold change) > 1.2; $P < 0.05$) in MFSD7C-KO HuLEC-5A cells versus control. Seahorse analysis of cellular oxygen consumption rate (OCR) (**b**), ATP production (**c**) in AMs isolated from the lung of $7C^{flox/flox}$, $7C^{-/-}$, and hemolytic mice. $n = 3$. **d** Lipid ROS production in AMs were determined by flow cytometry using C11-Bodipy. $n = 3$. **e** Mitochondrial ROS measured by MitoSOX green in AMs. **f** ATP luminescent levels of WT, 7C-KO1, 7C-KO2 and 7C-Rescued HuLEC-5A cells. Right: Western blot analysis of MFSD7C knockout and rescue efficiency. $n = 3$. **g** Immunofluorescence analysis of JC-1-stained WT, MFSD7C-KO, and rescued HuLEC-5A cells for the detection of mitochondrial membrane potential changes. Monomer in green, Aggregate in red, and nuclei in blue, photomicrograph bar = 5 μm. Right: quantification of fluorescence intensity. $n = 3$. **h** Uptake of long chain FAs (Bodipy c16) in HuLEC-5A cells was determined by FACS analysis. $n = 3$. **i** Volcano plot showing changes in lipid profile in AMs from $7C^{-/-}$ mice versus $7C^{flox/flox}$ mice. Right: indicated lipid screened by the variable importance in the projection VIP > 1. **j** Volcano plots showing the changes in TG, PE, PE(P) and PE(O). Changes were grouped as PUFA (red fill) and SFA/MUFA (white fill). Data are presented as mean + standard deviation (SD). $^*p < 0.05$; $^{**}p < 0.01$; $^{***}p < 0.001$; $^{****}p < 0.0001$.

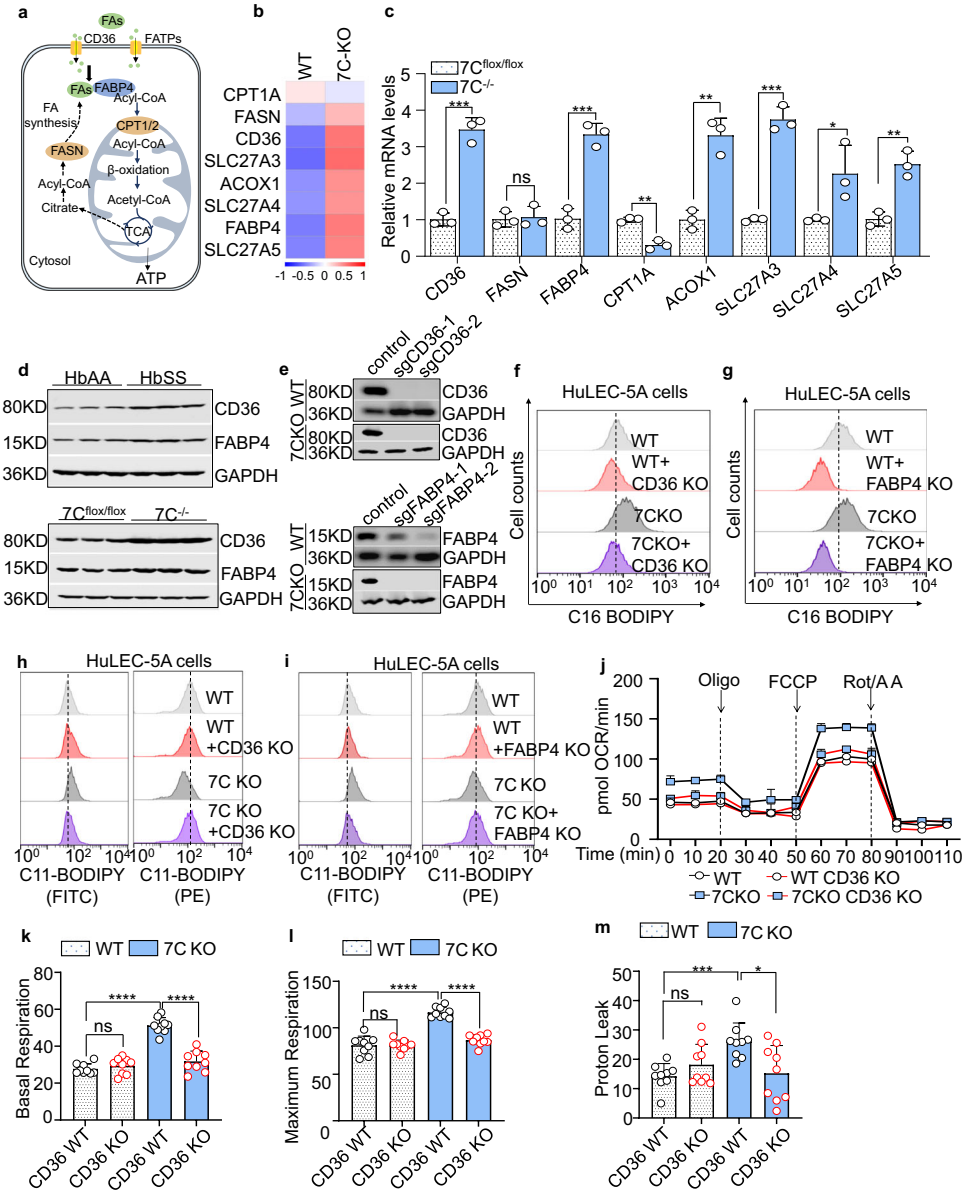

Fig. 5 | MFSD7C deficiency increased lipid flux by inducing CD36 and FABP4 expression. a Schematic diagram for fatty acid transportation and oxidation. **b** Heatmaps of relative gene expression in MFSD7C-KO HuLEC-5A cells versus control. **c** RT-qPCR analysis of CD36, FASN, FABP4, CPT1A, SLC27A3, SLC27A4, SLC27A5 and ACOX1 relative mRNA levels in AMs from $7C^{flox/flox}$ and $7C^{-/-}$ mice. $n = 3$. **d** Representative western blot of CD36 and FABP4 expression in AMs. Three biological replicates were performed for each sample. **e** Western blot analysis of CD36 and FABP4 knockout efficiency in MFSD7C-WT and KO HuLEC-5A cells. Three biological replicates were performed for each sample. Uptake of long chain FAs (Bodipy C16) in CD36 KO (**f**) or FKBP4 KO (**g**) HuLEC-5A cells was determined by FACS analysis. **h**–**i** Lipid ROS production in HuLEC-5A cells were determined by flow cytometry using BODIPY C11. Seahorse analysis of cellular oxygen consumption rate (OCR) (**j**), basal respiration (**k**), maximum respiration (**l**), and proton leak (**m**) in CD36 KO HuLEC-5A cells. $n = 3$. Data are presented as mean + standard deviation (SD). $^*p < 0.05$; $^{**}p < 0.01$; $^{***}p < 0.001$; $^{****}p < 0.0001$.

https://doi.org/10.1038/s41467-024-52537-6

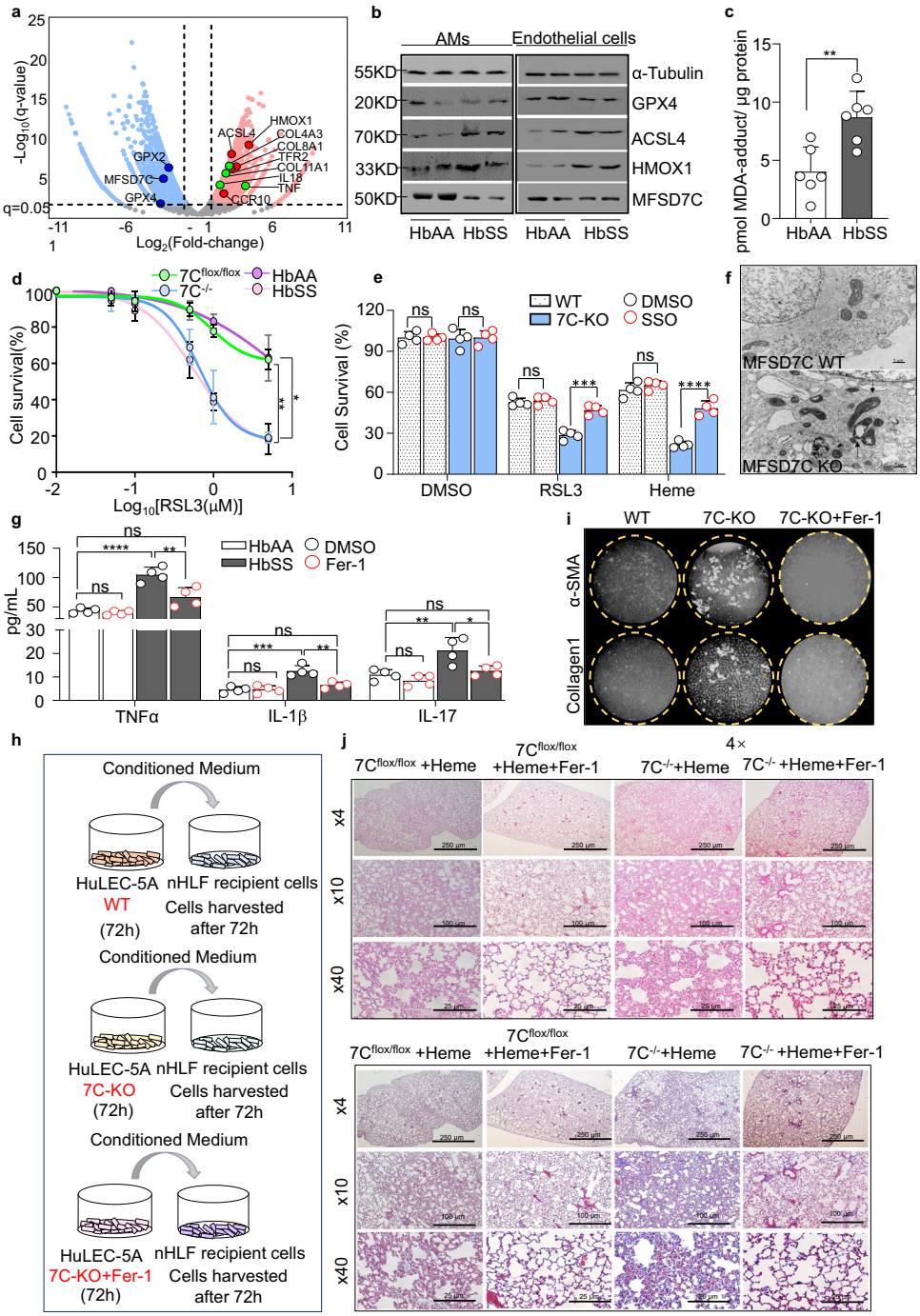

Fig. 6 | Lipid peroxidation contributes the ferroptosis sensitivity caused by MFSD7C deficiency. a Volcano plot illustrating DEGs in MFSD7C-KO HuLEC-5A cells versus control, highlighting ferroptosis related genes. **b** Representative western blot of GPX4, ACSL4, HMOX1 and MFSD7C expression in AMs and endothelia cells from lung tissues of 12-month-old HbAA and HbSS mice. Four biological replicates were performed for each sample. **c** MDA levels in lung tissues were assessed by TBARS assay. $n = 6$. **d** Cell viability of AMs treated with an increasing RSL3 concentration (0.01–5 μM) for 24 h. $n = 3$. **e** DMSO or CD36 inhibitor (SSO) (20 μM, 12 h) pretreated WT and MFSD7C-KO HuLEC-5A cells were treated with RSL3 (1 μM), Heme (10 μM) and DMSO (control) for 24 h and cell viability was analyzed. $n = 4$. **f** Representative electron microscope images of WT and MFSD7C-KO HuLEC-5A cells treated with RSL3 (1 μM) for 8 h, with arrows indicating mitochondria. Three biological replicates were performed for each sample. **g** Cytokine levels, including TNFα, IL-1β, and IL-17 in murine BALF were measured by ELISA with DMSO or Fer-1(1 μM) pretreatment for 12 h. $n = 4$. **h** Conditioned medium (CM) of RSL3 (0.5 μM) treated MFSD7C-KO and WT HuLEC-5A cells were collected after 72 h and transferred to recipient nHLFs for 72 h. Cells were pretreated with DMSO or Fer-1 (1 μM) for 1 h before RSL3 treatment. **i** ECM deposition assay in nHLFs exposed to MFSD7C-KO or WT HuLEC-5A cells derived CM. $n = 3$. **j** H&E staining and Masson's trichrome staining (x4, x10, x40) of lung tissues were shown. Three biological replicates were performed for each sample. Data are presented as mean + standard deviation (SD). $^{*}p < 0.05$; $^{**}p < 0.01$; $^{***}p < 0.001$; $^{****}p < 0.0001$.

on fibrosis. The HuLEC-5A cells were cultured in the presence and absence of Fer-1, then conditioned mediums were collected and applied in normal human lung fibroblasts (nHLF) recipient cells culture (Fig. 6h). Fluorescence imaging revealed excessive deposition of extracellular matrix, including α-SMA and collagen, in nHLF cell culture in response to MFSD7C knockout HuLEC-5A cells (Fig. 6i). Furthermore, extracellular matrix deposition was prevented in the presence of Fer-1 in MFSD7C knockout HuLEC-5A cells culture,

suggesting the unique role of MFSD7C in regulating fibrosis via preventing ferroptosis (Fig. 6i, Fig. S6k). Together, the MFSD7C deficiency enhanced ferroptosis promotes inflammation and fibrosis in vitro.

To explore the contribution of hemolysis-induced ferroptosis towards the lung inflammation and fibrosis in vivo, we pretreated the $7C^{flox/flox}$ and $7C^{-/-}$ mice with vehicle or ferroptosis inhibitor Fer-1 and then subjected to excess heme challenge (Fig. S6l). We found that MFSD7C knockout significantly exacerbated excess heme-induced lung damage phenotype, which is characterized by increased inflammation and fibrosis (Fig. 6j and Fig. S6m, n), suggesting the protect role of MFSD7C for hemolysis-induced lung injury. Not surprisingly, Fer-1 administration corrected the excess heme-induced lung damage and ferroptosis in both $7C^{flox/flox}$ and $7C^{-/-}$ mice (Fig. 6j, k and Fig. S6k–o). These results indicate that heme-induced ferroptosis is the driver of lung damage and MFSD7C knockout promotes the cell susceptibility.

Administration of MFSD7C mRNA improves lung damage in $7C^{-/-}$ mice

As MFSD7C demonstrated a critical role in pulmonary impairment under hemolytic conditions, we next translate the above discoveries into a therapeutic approach. We systematically delivered MFSD7C mRNA-loaded nanoparticles into hemolytic mice and their corresponding controls. Nanoparticles loaded with MFSD7C and/or luciferase mRNA were synthesized using 113-N16B with cholesterol, phospholipid, and mPEG2000-DMG, illustrated in the schematic diagram (Fig. 7a, Fig. S7). Bioluminescence imaging confirmed the lung-specific delivery of nanoparticles encapsulating luciferase mRNA, with explicitly increased luminescence intensity in the lung (Fig. 7b). In line with this result, the expression level of MFSD7C was elevated in the lung of mice administrated with MFSD7C mRNA-loaded nanoparticles (Fig. 7c and Fig. S8a).

$7C^{-/-}$, $7C^{flox/flox}$, HbSS-Townes, and HbAA-Townes mice received MFSD7C or control mRNA-loaded nanoparticles weekly for four weeks and were sacrificed for analysis on day 28 (Fig. 7d). $7C^{-/-}$ and $7C^{flox/flox}$ mice were additionally injected with 50 mg/kg of PHZ on day 0 and day 7 to induce hemolysis (Fig. 7d). IHC analysis confirmed that the administration of MFSD7C mRNA restored MFSD7C protein expression in $7C^{-/-}$ mice, while the BALF protein level remained unaltered (Fig. S8b, c). In agreement with the in vitro findings, the administration of MFSD7C mRNA-loaded nanoparticles ameliorated pulmonary inflammation in $7C^{-/-}$ mice, which was confirmed by the attenuated immune cell infiltration and proinflammatory cytokines production (Fig. 7e, f, Fig. S8d). Moreover, the increased number of neutrophils in BALF was significantly reduced in MFSD7C mRNA-treated $7C^{-/-}$ mice (Fig. S8e). Meanwhile, MFSD7C mRNA treatment attenuated fibrosis in $7C^{-/-}$ mice, as the high levels of collagen deposition and fibrosis-related gene expression were diminished in the MFSD7C mRNA-treated mice (Fig. 7g, h, Fig. S8f). MFSD7C mRNA also induced a similar recovery pattern in HbSS-Townes mice, characterized by reduced proinflammatory cytokines production, diminished neutrophil infiltration, and decreased fibrosis-related gene expression (Fig. S8g–j). Together, MFSD7C mRNA-loaded nanoparticles demonstrated their ability to improve hemolytic-induced lung damage in the MFSD7C knockout and hemolytic mice.

Next, we further evaluated the therapeutic mechanism of MFSD7C mRNA-loaded nanoparticles in the hemolytic mice model. MFSD7C mRNA significantly prevented RSL3-induced cell death of alveolar macrophages and endothelial cells isolated from $7C^{-/-}$ and HbSS-Townes mice (Fig. S8k, l). Furthermore, high lipid uptake and peroxidation in alveolar macrophages and endothelial cells isolated from $7C^{-/-}$ and HbSS-Townes mice were suppressed by the MFSD7C mRNA treatment, confirming the protective role of MFSD7C in hemolysis-induced lipid oxidative stress (Fig. 7i, j and Fig. S8m–p). At last, with the recovered MFSD7C expression, the level of HMOX1, ferroptosis-related gene *ACSL4* and MDA were downregulated while the antioxidant gene *GPX4* was restored (Fig. 7k, Fig. S8q–s). With these results, we confirmed that the administration of MFSD7C protected the mice from hemolytic-induced lung damage by preventing oxidative stress and inhibiting ferroptosis.

Discussion

Lipid peroxidation and iron accumulation are the necessary inducers for ferroptosis. The accumulation of lipid peroxides compromises cellular membrane fluidity, permeability, and eventually resulting in cell death[19]. During hemolytic disorders, the accumulation of circulating heme leads to iron accumulation and catalyses ROS production, resulting in imbalanced redox reactions in the cells. Thus, hemolysis can induce ferroptosis. Latest studies have demonstrated the relationship between excess heme and ferroptosis in human platelet and breast cancer cells[6,20]. Here, we systematically studied the mechanisms that underlie the excess heme- induced lung damage of SCD mice. The data show that excessive heme release during hemolysis leads to the downregulation of MFSD7C. Loss of MFSD7C aggravates hemolytic-related lung damage symptoms, at least in part, through enhanced ferroptosis by the increased ROS and dysregulation of GPX4 and ACSL4. Correspondingly, intravenous administration of MFSD7C mRNA-loaded nanoparticles protects hemolytic mice from pulmonary damage.

MFSD7C can bind heme to switch the energy production from ATP synthesis to thermogenesis and had a pathological role in Flower-syndrome[12,14]. Deficiency of MFSD7C leads to impaired development of blood vessels in the embryonic brain[13]. However, despite being a heme partner, to date, no study has demonstrated the role of MFSD7C in hemolytic-related disease. Here, our results suggest that excessive heme release during hemolysis could lead to a downregulated MFSD7C expression in the hemolytic mice, especially in the lung (Figs. 1–2). With the reduction in MFSD7C expression, the cells are expected to protect from heme overload, which promotes iron accumulation and ROS production[5]. However, aggravated hemolytic-related lung damage was seen in mice with MFSD7C depletion (Fig. 3). Hence, these observations suggest that MFSD7C may possess an alternative mechanism which protects the mice from hemolysis complications.

Our previous study highlighted the role of MFSD7C in regulating mitochondrial energy metabolism in response to intracellular heme levels[14]. Under conditions of low heme levels, MFSD7C facilitates ATP synthesis. Upon binding with heme, MFSD7C dissociates from the electron transport chain components and SERCA2b, switching the energy production from ATP synthesis to thermogenesis[14]. In line with this study, we found that MFSD7C deficiency reduced ATP production and altered mitochondrial morphology in alveolar macrophages and endothelial cells (Fig. 4). Fatty acid uptake by the cells was upregulated to fulfil the insufficient energy production due to impaired mitochondrial function. Indeed, our data demonstrated that MFSD7C depletion led to an elevated intracellular abundance of PUFA and lipid peroxidation in the cells. Together, these findings highlight the importance of MFSD7C in maintaining normal metabolism pathways, protecting the cells from oxidative cellular damage caused by lipid peroxidation. Mechanistically, we found that MFSD7C deficiency promoted lipid influx by inducing CD36 and FABP4 expression (Fig. 5). A previous study in the lab has identified the interaction between MFSD7C and fatty acid mitochondrial transporter CPT1/2[14]. Hence, we speculated that the loss of MFSD7C disables mitochondrial translocation via CPT1/2, thereby inhibiting fatty acid metabolites entering the TCA cycle and energy production. To overcome the insufficient mitochondrial lipid β-oxidation, the cells are urged to increase lipid uptake by promoting CD36 and FABP4 expression, thus enhancing the accumulation and peroxidation of lipid in the cells. However, further experiments are required to confirm the role of CPT1/2 in lipid remodeling in MFSD7C-deficient cells.

https://doi.org/10.1038/s41467-024-52537-6

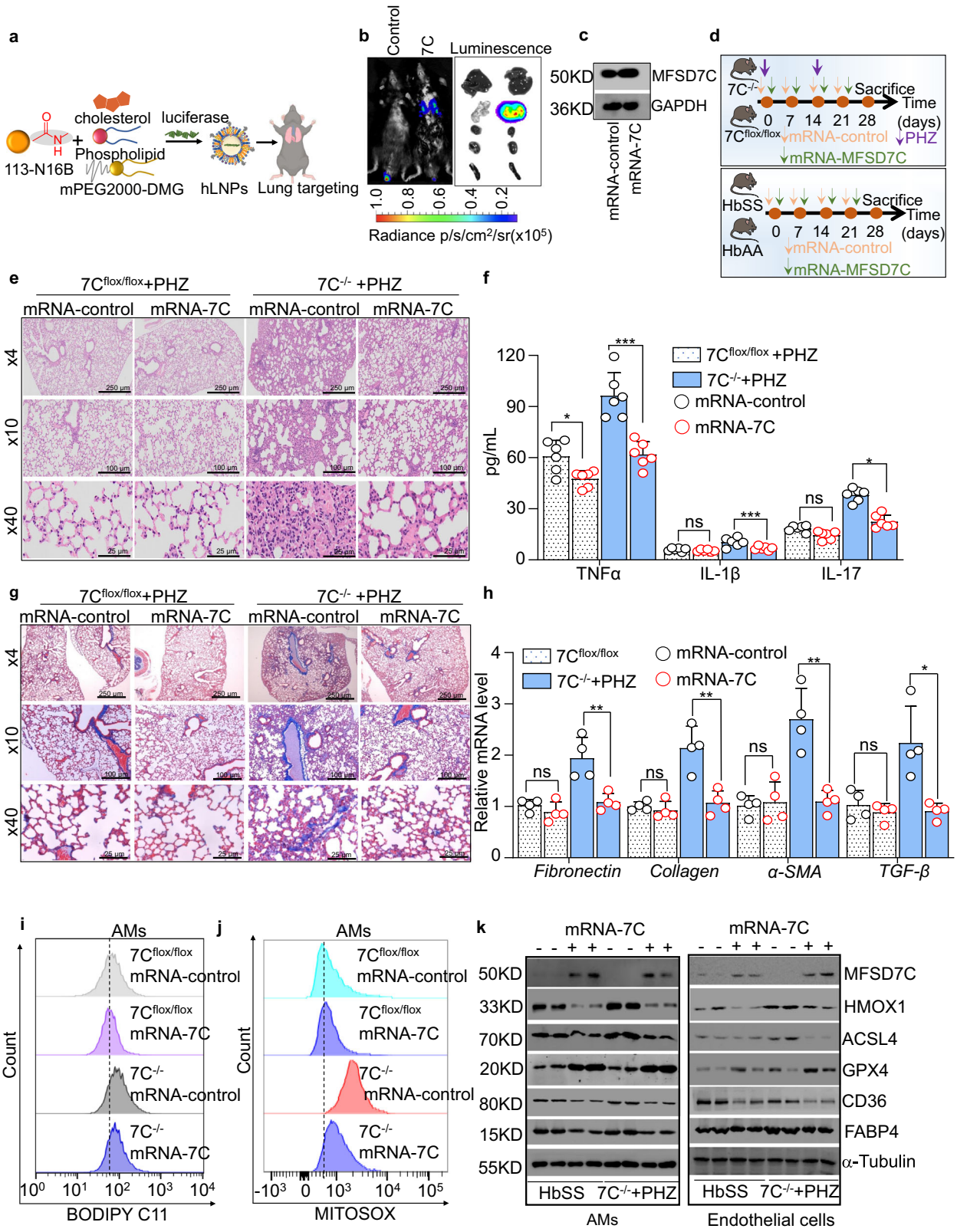

As previously reported, oxidation of PUFA, particularly arachidonic acid, led to ferroptosis and acute liver failure in mice, which was rescued by ferroptosis inhibitor Fer-1[21]. Similarly, upregulation of arachidonic acid and lipid peroxidation were seen in MFSD7C knockout HuLEC-5a cells and lung tissues of *7C*$^{-/-}$ mice and HbSS mice (Fig. 5). Furthermore, the pro-ferroptotic gene ACSL4, which is involved in lipid metabolism, showed significant upregulation, while the central ferroptosis inhibitor GPX4 exhibited decreased expression in AMs and endothelia cells from lung tissues of *7C*$^{-/-}$ mice and HbSS mice. These findings suggest that ACSL4 and GPX4 is responsible for the initiation of ferroptosis mediated by hemolysis or MFSD7C deficiency (Fig. 6 and S6). Meanwhile, our results suggest that severe ferroptosis leads to intense pulmonary inflammation and fibrosis in the mice suffering from hemolysis (Fig. 6), strengthening the evidence for the

Fig. 7 | Administration of MFSD7C mRNA improves lung damage in $7C^{-/-}$ mice. **a** Schematic illustration of lung targetability of hybrid 113-N16B lipid nanoparticles. hLNP was formulated by 113-N16B: cholesterol: phospholipids: DMG-PEG2000 (50:38.5:10:1.5). **b** Representative whole-body and organs bioluminescence images of mice by IVIS imaging system. Mice were intravenously administered with Control mRNA-loaded hLNPs or Luc+*7C* mRNA-loaded hLNPs at a single dose of 0.5 mg/kg. Images were taken at 6 h post injection. **c** Western blot analysis of MFSD7C expression in lung of $7C^{flox/flox}$ mice treated with *7C* mRNA-loaded hLNPs at 6 h post injection. Three biological replicates were performed for each sample. **d** Treatment design for hemolytic mice and SCD mice. 12-month old HbAA- and HbSS-Townes mice and 8-week old $7C^{flox/flox}$ and $7C^{-/-}$ mice ($n = 6$) received MFSD7C or control mRNA-loaded nanoparticles weekly for four weeks and were sacrificed for analysis at one week after last treatment. $7C^{-/-}$ and $7C^{flox/flox}$ mice were additionally injected with 50 mg/kg of PHZ on day 0 and day 7 to induce hemolysis. **e** H&E staining of lung tissues (x4, x10, x40). **f** Cytokine levels, including TNFα, IL-1β, and IL-17 in murine BALF were measured by ELISA. $n = 4$. **g** Masson's trichrome staining of lung tissues (x4, x10, x40). **h** Changes in the mRNA expression of Fibronectin, Collagen, α-SMA, and TGF-β were evaluated by RT-qPCR. $n = 3$. **i** Lipid ROS production in AMs were determined by flow cytometry using BODIPY C11. **j** Mitochondrial ROS measured by MitoSOX green in AMs. **k** Representative western blot of MFSD7C, HMOX1, ACSL4, GPX4, CD36 and FABP4 expression in AMs and endothelial cells isolated from HbSS-Townes mice and PHZ-challenged $7C^{-/-}$ mice treated with MFSD7C mRNA or control mRNA. Data are presented as mean + standard deviation (SD). $^{*}p < 0.05$; $^{**}p < 0.01$; $^{***}p < 0.001$; $^{****}p < 0.0001$.

pathological role of ferroptosis in the hemolytic lung. Our study also suggests the anti-ferroptotic role of MFSD7C, which protect the mice from hemolytic-related lung damage. Considering the intimate relationship between ferroptosis and lipid peroxidation, mitochondria might play a critical role in regulating ferroptotic cell death. During ferroptosis, mitochondria is morphologically altered, characterizing by extensive shrinkage, increased membrane density and loss of mitochondrial cristae[22,23]. Alteration in multiple mitochondrial metabolism pathways (reviewed elsewhere[24]) directly affects cell sensitivity toward ferroptosis. Upon MFSD7C depletion, altered mitochondrial structure was observed and the cells were sensitized to ferroptosis upon administering ferroptosis-specific inducer or heme (Fig. 6). Together, in the context of MFSD7C deficiency, the accumulation of lipid peroxidation induced by mitochondria dysfunction and the dysregulation of ACSL4 and GPX4 in the cells enhances the ferroptosis of the pulmonary cells and leads to lung damage under hemolytic conditions. Further studies are required to explore the detailed mechanisms underlying the dysregulation of ACSL4 and GPX4 induced by MFSD7C deficiency.

The key finding in this paper is the intravenous administration of MFSD7C mRNA-loaded nanoparticle protects mice against hemolytic-related lung damage (Fig. 7). mRNA was delivered in mice via a polymer-lipid nanoparticle with the combination of PBAEs and PEG, which has previously demonstrated its ability to deliver mRNA to the lung[25]. By using the MFSD7C mRNA-loaded nanoparticles, we successfully restored MFSD7C expression level in mice, preventing lipid peroxidation and ferroptosis, and thereby alleviating hemolytic-induced lung damage. Owning these results, we further confirmed that MFSD7C holds a protective role in mice with hemolytic conditions.

Regulating lipid remodeling to mediate ferroptosis is a potential therapeutic strategy in a variety of pathological scenarios. In addition to lung, ferroptosis was found to trigger liver damage, including acute liver failure, chronic liver injury and fibrosis[26]. Several lipophilic antioxidants, such as Fer-1 and CoQ_{10}, prevent lipid peroxidation and inhibit ferroptosis via radical binding[7,27]. Treatment of lipophilic antioxidants was shown to effectively alleviate liver damage in mouse models with liver diseases[7,28]. However, none are used in clinical settings due to their inadequate pharmacokinetic or pharmacodynamic profiles[29]. Our study shows that MFSD7C protects hemolysis-induced lung impairments through preventing lipid peroxidation and ferroptosis, suggesting that MFSD7C is a potential therapeutic target for the development of improved treatment strategies (Fig. 8).

In summary, we demonstrated a mechanism of MFSD7C through which suppresses ferroptosis susceptibility by maintaining mitochondrial function and the expression of ferroptosis regulators, ACSL4 and GPX4. Moreover, our study suggests that direct MFSD7C mRNA supplement protects alveolar macrophage and pulmonary endothelial cells from ferroptosis, alleviating hemolytic-induced lung damage. From a clinical perspective, these findings indicate that treating SCD patients by inhibiting ferroptosis or MFSD7C administration may help prevent hemolysis induced lung injury. Future studies are needed to test the potential clinical implications of this therapeutic strategy. Although acute chest syndrome (ACS) is an acute lung injury syndrome that occurs frequently in patients with SCD, much less is known about the lung fibrosis phenotype until now. Therefore, further studies are required to evaluate the protect role of MFSD7C in the lung injury syndrome of patients with SCD in the future.

Methods

Mice

Conditional *Mfsd7c* knockout mice (B6/JGpt-*Flvcr2*^{em1Cd}/Gpt mice, $7C^{flox/+}$) were purchased from Gempharmatech (stock no. T034000). Mice carrying the *Mfsd7c* allele were maintained on a C57BL/6JGpt background in specific pathogen-free conditions. B6;129-Hbb$^{tm2(HBG1,\ HBB^{*})Tow}$/Hbb$^{tm3(HBG1,\ HBB)Tow}$Hba^{tm16Tow}/J mice (stock no. 013071) were purchased from the Jackson Laboratory. Both female and male mice were utilized in the mice mentioned above[14,30,31]. With the approval of the Laboratory Animal Ethical and Welfare Committee of Shandong University Cheeloo College of Medicine, mice were kept in the animal facility at Shandong University, with a standard 14:10-h light: dark cycle, ambient temperature of 23-25 °C, humidity levels of 40-70% and full access to water and facility chow, following the guidelines set forth by the Animal Care and Utilization Committee of Shandong University, China. Finally, all mice were euthanized by cervical dislocation under 3% isoflurane anesthesia.

Cell line

Experiments were performed in HuLEC-5A cells (Procell Corporation, CL-0565), which were cultured in MCDB131 medium containing 10% FBS (Gibco), 10 ng/mL EGF, 1 μg/mL Hydrocortisone, 10 mM L-glutamine, 1% penicillin-streptomycin (HyClone, SV30010) and maintained in humidified 5% CO_2 incubator at 37 °C if not indicated otherwise.

Generation of *Mfsd7c* conditional-knockout mice

Mice carrying a tamoxifen-inducible Cre-recombinase (UBC-Cre) (stock no. 007001) were crossed with $Mfsd7c^{flox/flox}$ mice to generate mice carrying both alleles ($Mfsd7c^{flox/+}$; UBC-Cre). $Mfsd7c^{flox/+}$; UBC-Cre mice were crossed to $Mfsd7c^{flox/flox}$ to generate $Mfsd7c^{flox/flox}$; UBC-Cre mice. Genotyping was performed using specific primers for Cre and $Mfsd7c^{flox}$ (Supplementary Table S1). To induce cre expression, 6-to 8-week-old $Mfsd7c^{flox/flox}$; UBC-Cre mice were injected intraperitoneally with 75 mg/kg tamoxifen (T5648, Sigma-Aldrich) daily for five times. The day of the first tamoxifen injection was defined as day -11. *Mfsd7c* knockout efficiency was confirmed by western blotting using anti-MFSD7C antibody on day 0.

To construct the hemolytic mouse model, $7C^{flox/flox}$ and $7C^{-/-}$ mice were injected intraperitoneally with PHZ (50 mg/kg) on days 0 and 14. Hemolytic mice were euthanized on day 28 for further analysis.

Murine endothelial and epithelial cells isolation

Endothelial cells were isolated from mouse lung tissue using endothelial cell isolation kit (Miltenyi Biotec, 130-109-680) following the manufacturer's protocols. Briefly, mice lung tissues were transferred into a 50 mL tube containing 25 mL collagenase and incubated at 37 °C for one hour occasionally shaking mixture. After filtering by a 70 μm

https://doi.org/10.1038/s41467-024-52537-6

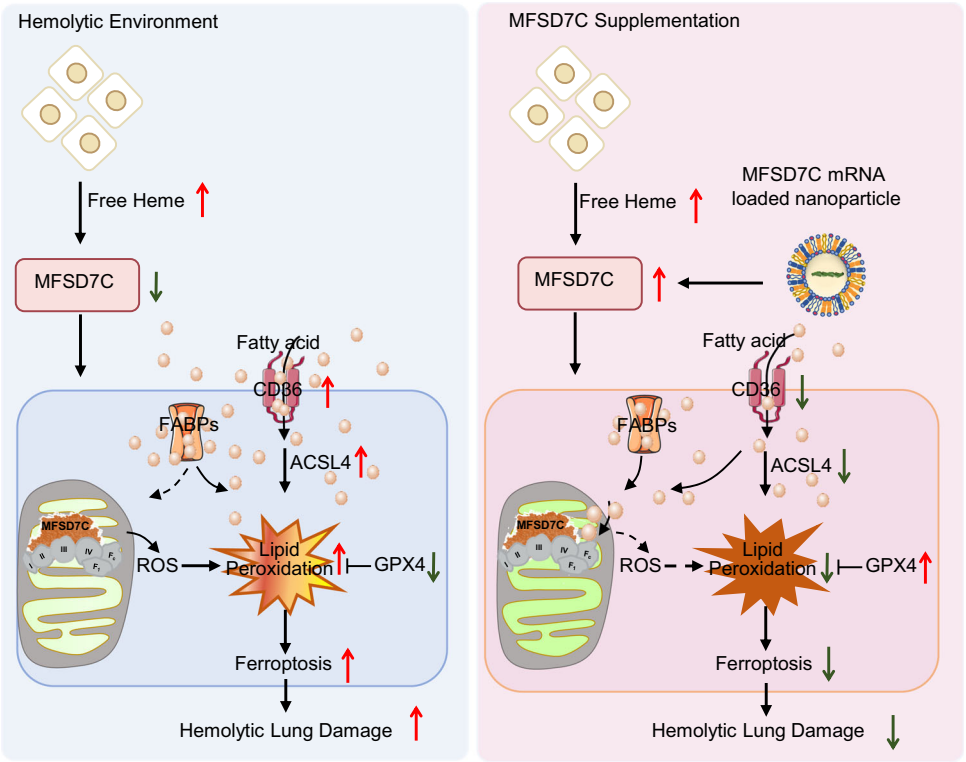

Fig. 8 | MFSD7C protects hemolysis-induced lung impairments by inhibiting ferroptosis. Elevated levels of free heme in serum due to hemolysis led to a reduction in MFSD7C expression in AMs and endothelial cells within lung tissue of mice. The decrease of MFSD7C promotes the uptake of fatty acid by CD36. Meanwhile, the downregulation of MFSD7C causes mitochondria dysfunction and dysregulation of ACSL4 and GPX4, which promotes lipid peroxidation and triggers ferroptosis, resulting in hemolytic lung damage. Intravenous administration of MFSD7C mRNA-loaded nanoparticles can restore MFSD7C protein levels, mitigating ferroptosis, and thereby alleviating hemolytic-induced lung damage.

disposable cell strainer, the mixture was centrifuged at 125 g for 5 min at 4 °C. Pellet was resuspended and incubated with the lung non-endothelial cell depletion cocktail for 15 min in 4 °C, following magnetic separation to acquire lung endothelial cells. For purity assessment of lung endothelial cells, cells were stained with CD90.2-APC (Cat# 130-091-790, Miltenyi Biotec) and CD31-PE (Cat# 130-097-422, Miltenyi Biotec) and analysed by flow cytometry.

Epithelial cells were isolated from mouse lung using EasySep™ Mouse Epithelial Cell Enrichment Kit II (STEMCELL, Cat# 19868) following the manufacturer's protocols. For purity assessment of lung epithelial cells, started and enriched cells were stained with PE Goat anti-rat IgG (minimal x-reactivity) Antibody (BioLegend, Cat# 405406) labeling any residual non-epithelial cells and analysed by flow cytometry.

BALF acquisition, AMs Isolation and BALF cytokines

BALF was obtained by perfusing 0.1 M NaCl as described previously[32]. BALF samples were centrifuged at 140 × *g* for 10 min at 4 °C. For alveolar macrophages (AMs) isolation, the pellet was resuspended with RPMI-1640 medium as described previously[33]. Cells were cultured in an incubator at 37 °C, 5% CO_2 for 2 h, and then removed suspended impurities to obtain pure primary AMs for further experiments. BALF supernatants were then aliquoted and stored at -80 °C for ELISA. The levels of TNFα, IL-1β, and IL-17 in murine BALF were quantified using ELISA kits (Beyotime, PT512, PI301, and PI545, China) according to the manufacturer's instructions.

Generation of MFSD7C-KO and MFSD7C-Rescued stable cell lines

CRISPR/Cas9 was used to knockout MFSD7C in HuLEC-5A cells. Guide RNA sequences used within this study were designed using the online tool CRISPR Design. gRNA-1 and gRNA-2, specific for human MFSD7C, were inserted in BsmBI site of the lentiCRISPR-v2 vector (puro). All the final constructs were confirmed by sequencing.

MFSD7C-KO1-F: 5′- CTCGTCCCGGTCTTCAATGT-3′
MFSD7C-KO1-R: 5′- ACATTGAAGACCGGGACGAG -3′
MFSD7C-KO2-F: 5′- GAACCTAAGTATGAGGCATC -3′
MFSD7C-KO2-R: 5′- GATGCCTCATACTTAGGTTC -3′

Lentiviral production and transduction were performed as described previously[14]. Briefly, lentiCRISPR-V2 (puro)-MFSD7C plasmid or lentiCRISPR-v2 (puro)-Control, psPAX2 plasmid (packaging, Addgene Cat# 12260) and the pMD2.G plasmid (envelope, Addgene Cat# 12259) were co-transfected into 293 T cells with jetOPTIMUS® DNA Transfection Reagent (101000006, Polyplus). Lentiviruses were harvested after transfection for 24 hours and 48 hours. For lentiviral transduction, 1×10^5 HuLEC-5A cells were seeded into a 12-well plate. Lentivirus was transduced with 10 μg/mL polybrene (Beyotime, C0351) for 24 h. Transduced cells were selected by 1 μg/mL puromycin for 48 h. Monoclonal cell population were isolated by limiting dilution and expanded.

2×10^5 HuLEC-5A MFSD7C KO2 cells were seeded in 6-well plate for 24 h prior to transfection. PCDH-copGFP-MFSD7C plasmid was constructed by homologous recombination. $MFSD7C^{p.G878A}$ construct was generated by Mut Express II Fast Mutagenesis Kit V2 (Vazyme, Cat# C214-01) and PCDH-copGFP-MFSD7C plasmid as template. PCDH-copGFP-$MFSD7C^{p.G878A}$ plasmid was used to block CRISPR/Cas9 mutation of MFSD7C and followed by lentivirus package assay as described above. For infection, MFSD7C lentivirus was added to cell medium with 10 μg/mL polybrene for 12 h. The stably genetic MFSD7C rescued cells were selected by flow cytometry.

Synthesis of 113-N16B

113-N16B was synthesized according to the literature[34]. To a solution of 2-Aminoethanethiol hydrochloride (13.218 g, 60 mmol) in 60 mL of

methanol was added a solution of 2,2′-dithiodipyridine (3.408 g, 30 mmol) in 30 mL of methanol, followed by the addition of 2.4 mL of acetic acid. The mixture was stirred at room temperature under the atmosphere of argon for 40 h. To the solution was added 100 mL of sat. $NaHCO_3$. The mixture was then extracted with chloroform/isopropanol (3:1). The combined organic layer was washed with brine, dried over *anhyd*. Na_2SO_4 and concentrated *in vacuo*. The residue was purified by column chromatography to give compound **S1** as a yellow oil (2.468 g, 13.3 mmol, 44%). The spectra of **S1** were the same as previously reported[35].

To a solution of **S1** (50 mg, 0.268 mmol) in 10 mL of dichloromethane (DCM) was added 1-Dodecanethiol (65.2 mg, 0.322 mmol) and acetic acid (32.1 mg, 0.536 mmol). The mixture was stirred at room temperature overnight. The reaction was quenched by the addition of 1 mL of sat. $NaHCO_3$. The mixture was extracted with dichloromethane. The combined organic layer was dried over *anhyd*. Na_2SO_4 and concentrated *in vacuo*. The residue was purified by column chromatography to give compound **S2** (10.5 mg, 0.0317 mmol, 14%). ^{1}H NMR (400 MHz, $CDCl_3$) δ (ppm) 3.01 (m, J = 6.1 Hz, 2H), 2.76 (m, 2H), 2.68 (m, 2H), 1.67 (m, 2H), 1.37 (m, 2H), 1.26 (m, 16H), 0.88 (t, J = 6.7 Hz, 3H). ^{13}C NMR (100 MHz, $CDCl_3$) δ (ppm) 40.4, 40.1, 39.1, 32.1, 29.8, 29.8, 29.7, 29.7, 29.5, 29.4, 29.3, 28.7, 23.0, 14.4.

To a solution of compound **S2** (462 mg, 1.66 mmol) in 60 mL of DMF at 0 °C was added acryloyl chloride (301.34 mg, 3.33 mmol) and triethylamine (337 mg, 3.33 mmol). The mixture was stirred at 0 °C for another 2 h and was then quenched with sat. NH_4Cl. The mixture was extracted with ethyl acetate. The combined organic layer was washed with brine, dried over *anhyd*. Na_2SO_4 and concentrated *in vacuo*. The residue was purified by column chromatography to give compound **S3** (321 mg, 0.968 mmol, 58%) ^{1}H NMR (400 MHz, $CDCl_3$) δ (ppm) 6.30 (dd, J = 17.0, 1.4 Hz, 1H), 6.10 (dd, J = 17.0, 10.3 Hz, 1H), 5.97 (br, 1H), 5.66 (dd, J = 10.3, 1.4 Hz, 1H), 3.69 (m, 2H), 2.83 (m, 2H), 2.69 (m, 2H), 1.67 (m, 2H), 1.36 (m, 2H), 1.27 (m, 16H), 0.88 (t, J = 6.6 Hz, 3H). ^{13}C NMR (100 MHz, $CDCl_3$) δ (ppm) 165.7, 130.8, 126.8, 39.0, 38.2, 37.7, 32.0, 29.8, 29.8, 29.7, 29.6, 29.5, 29.3, 29.3, 28.6, 22.8, 14.3.

A mixture of compound **S3** (100 mg, 0.302 mmol) and 2,2′-Diamino-N-methyldiethylamine (7.0 mg, 0.0604 mmol) was stirred at 90 °C under the atmosphere of Argon. The reaction mixture was purified by column chromatography to give compound **113-N16B** (7.1 mg, 0.00493 mmol, 8.2%). **MS** (m/z): calculated for $C_{73}H_{148}N_7O_4S_8$ $[M+H]^+$ 1442.9, found: 1443.2; calculated for $C_{73}H_{149}N_7O_4S_8$ $[M+2H]^{2+}$ 722.0, found: 722.4.

Hybrid 113-N16B lipid nanoparticles preparation

Hybrid 113-N16B lipid nanoparticles (LNPs) were prepared as described previously[34]. Briefly, 113-N16B were synthesized and then rapidly mixed with cholesterol, phospholipids and DMG-PEG2000 at a molar ratio of 50:38.5:10:1.5 in ethanol solution with sodium acetate buffer (pH 5.2, 25 mM) which contains targeting mRNA. Next, hLNPs were further dialyzed against phosphate-buffered saline (PBS) (10 mM, pH 7.4) in 3,500 MWCO (molecular weight cut off) cassettes (Thermo Fisher Scientific) overnight at 4 °C.

The administration of Mfsd7c mRNA loaded hLNPs in the hemolytic mouse model

8-week-old *Mfsd7c*$^{flox/flox}$ and *Mfsd7c*$^{-/-}$ mice were administrated by intraperitoneal (i.p.) injection of 50 mg/kg phenylhydrazine (PHZ, 114715, Sigma-Aldrich) on days 0 and 14 to establish hemolytic mouse model[36]. Meanwhile, Mfsd7c mRNA-loaded nanoparticles (0.5 mg/kg) were administrated through tail vein injection on days 0, 7, 14, and 21, respectively. The mRNA-control groups received the same amount of control mRNA-loaded nanoparticles at the same time points in the above hemolytic models. 6 mice were assigned per group unless otherwise stated. For the therapeutic experiments, a similar scheme was followed with HbSS-Townes and HbAA-Townes mice. All mice were euthanized at day 28 after PHZ treatment and subjected to further analyses. All experiments were performed in compliance with the Shandong University Animal Care and Use Ethics Committee.

Tissue preparation

Mice were euthanized on day 28, then ligated the lungs and excised immediately. Left lung lobes were frozen rapidly and stored at −80 °C for RT-qPCR, western blot analysis and MDA content measurement, whereas samples of the right lung lobes were submitted to histopathological and immunohistochemical evaluation under light microscopy. Other organs were also excised immediately, frozen rapidly and stored at −80 °C for RT-qPCR and western blot analysis.

Measurement of lung wet/dry ratio

For wet weights, the right lower lungs were obtained, and then weighed. For dry weights, they were incubated in an oven at 60 °C for 72 h. The wet/dry ratio was calculated using the wet and dry weights.

Serum Heme and Serum Hemopexin levels measurement

Blood samples were obtained from HbAA-Townes mice and HbSS-Townes mice, followed by peripheral blood extraction with standard venepuncture techniques, and centrifugation at 1200 *g* for 10 min at 4 °C. Serum heme levels were determined using QuantiChrom™ Heme Assay Kit (BioAssay, DIHM-250, Hayward, CA) following the manufacturer's protocols. Serum hemopexin level was measured using Hemopexin ELISA Kit (Aviva Systems Biology, OKIA00097) following the manufacturer's protocols. The remaining serum was frozen at −80 °C for further analyses.

Plasma total bilirubin levels measurement

Total bilirubin concentrations were determined by using QuantiChrom™ Bilirubin Assay Kit (BioAssay, DIBR-180) following the manufacturer's protocols.

RNA extraction and quantitative RT-qPCR

Lung tissue was homogenized using Trizol reagent (Takara, Japan). Total RNA was isolated by phenol-chloroform extraction. The exact quantity of total RNA (1 μg) was reverse-transcripted to cDNA (Accurate Biology, China) following the manufacturer's instructions. PCR amplification was performed using the SYBR-Green (Accurate Biology, China). To quantify transcription, the mRNA expression levels of the target genes were normalized to β-Actin. All samples were run in quadruplicates, and relative quantification was calculated following the 2-ΔΔCT method. All primer sequences are listed in Table S1.

Lysates, SDS-PAGE, and western blotting

Tissue and cell lysates were prepared as reported[14,37]. Primary antibodies specific for MFSD7C (Cat# HPA037984, Sigma), glutathione peroxidase 4 (GPX4) (Cat# SAB4300725, Sigma), acyl-CoA synthetase long-chain family member 4 (ACSL4) (Cat# PA5-89830, Thermo Scientific), heme oxygenase 1(HMOX1) (Cat# 10701-1-AP, Proteintech, USA), CD36 (Cat# 28109, CST), FABP4(Cat# #50699, CST), α-tubulin (Cat# 2148, Proteintech), β-actin (Cat# 700, CST), GAPDH (Cat# 5174, CST), were used in western blotting. Horseradish peroxidase-conjugated secondary antibody (CST, Cat# 7074 or Cat# 7076) was used at room temperature for 1 h and immunoreactive proteins were visualized by using ECL Basic Kit (Abclonal, RM00020, USA). For analysis, background intensity was subtracted from band intensity, and the proteins of interest were normalized to α-tubulin, β-actin or GAPDH using ImageJ Software.

Lung histology and immunohistochemistry (IHC) staining

Lung tissue was immediately placed in formalin for fixing overnight. After paraffin embedding, lungs were processed for histology, sectioned at 5 μm, and stained with hematoxylin and eosin (H&E) and

Masson's trichrome. For immunohistochemistry (IHC) staining, the lung sections were probed with polyclonal rabbit anti-MFSD7C as described previously[38]. Images of lung tissue slides were scanned by a Nano Zoomer Slide Scanner. Inflammation and fibrosis score was calculated as previously reported[39,40].

Immunofluorescence

Immunofluorescence staining was performed on paraffin-embedded mouse lung tissue as described previously[41]. Briefly, the slides were incubated with primary antibodies CD31 (Cat# ab222783, Abcam) or F4/80(Cat# ab6640, Abcam) overnight at 4 °C. Secondary antibodies were incubated with the slides for 1 h at room temperature, as follows: Rabbit anti-Mouse IgG (H + L) Cross-Adsorbed Secondary Antibody (Cat# A-11061, thermos fisher) and anti-rat IgG (H + L) antibody (Cat# 4417, CST). Finally, the slides were dyed in DAPI (Cat# D1306, thermos fisher) for 10 min. Pictures were acquired with LSM 780 confocal microscope (Olympus), and images were quantified using ImageJ. All the immunofluorescence experiments were performed at least three times independently, and the pictures shown in the figures were representative images of at least three experiments.

Oxygen consumption rate (OCR) measurements

AMs or lung endothelial cells were seeded in XF96 cell culture microplates (Seahorse Bioscience) and incubated in XF assay medium-modified DMEM. For OCR measurement, cells were analyzed according to the procedures described in the Seahorse XF Cell Mito Stress Test kit. Changes in oxygen consumption were measured following treatment with oligomycin (5 μM, MCE), FCCP (2 μM, MCE), and rotenone (1 μM, MCE) plus antimycin A (1 μM, MCE) (Rot/AA) using Seahorse XFe96 analysers.

RNA sequencing

The total RNA in AMs from MFSD7C-KO and WT HuLEC-5A cells was extracted using Trizol (Takara) and assessed using the RNA Nano 6000 Assay Kit of the Bioanalyzer 2100 system (Agilent Technologies, CA, USA). RNA-Seq libraries were prepared and sequenced by the Illumina NovaSeq 6000. The index of the reference genome was built using Hisat2 (v2.0.5), and paired-end clean reads were aligned to the reference genome.

Cell viability

HuLEC-5A cells, AMs and endothelial cell viability was determined using the MTT assay. 100 μL of cells were seeded in a 96-well plate at a density of 5000 cells per well. Next day, HuLEC-5A cells were incubated with 1 μM RSL3(cat# R407911, Aladdin) for 24 h. AMs and endothelial cells were treated with 10 μM heme (cat# H8130, Solarbio) for 24 h. Cells were incubated with 10 μL of MTT (5 mg/mL) each well at 37 °C in the dark for 4 h. 100 μL of dimethyl sulfoxide (DMSO) was added to dissolve formazan crystals. The optical density (OD) value was measured at 490 nm by a microplate reader. Cell survival rate was calculated subsequently. The experiments were performed in triplicate.

Measurement of arachidonic acid level

Arachidonic acid (AA) levels were quantified using an ELISA kit (Elabscience, E-EL-0051c) following the manufacturer's protocol. In brief, for HuLEC-5A cells, 10^6 cells per sample were gently washed with pre-cooled PBS, digested, and lysed by repeated freeze-thaw cycles in 150 μL of pre-cooled PBS. The resulting lysate was collected by centrifugation at 1500 × *g* for 10 min. In the case of mouse lung tissues, 50 mg of tissue was homogenized in 500 μL of PBS using a glass homogenizer on ice. Further cell disruption was achieved through sonication, followed by centrifugation at 5000 × *g* for 5-10 min at 2–8 °C to obtain the supernatant. The AA quantification process involved adding standard and test samples, enzymes, followed by incubation at 37 °C for 30 min, washing steps, color development, termination of the reaction, and measurement at 450 nm using a microplate reader. The AA levels were then calculated based on a standard curve and expressed as ng of AA per mg of protein.

Measurement of MDA content

Malondialdehyde (MDA) levels in lung tissue and HuLEC-5A cells were measured using Lipid Peroxidation (MDA) Assay Kit (Abcam, ab118970) in accordance with the manufacturer's instructions. In brief, 1–10 mg of lung tissue or HuLEC-5A cells were homogenized in Lysis Solution and centrifuged at 13,000 *g* for 10 min. Supernatant was harvested, and protein concentration was measured by BCA protein assay kit (Beyotime, P0010, China). Lung tissue or cell lysates were mixed with TBA reagent at 1:3 ratio. After incubating at 95 °C for 60 min, the mixture was cooled to room temperature in an ice bath for 10 min. To get the absorbance, 200 μL of mixture containing MDA-TBA adduct was added to a 96-well plate and measured at 532 nm with microplate reader. Finally, the MDA content was calculated according to the standard curve and shown by pmol MDA per μg protein.

Flow cytometry analysis of lipid ROS

Lipid ROS production was detected using BODIPY 581/591 C11 for lipid peroxidation assay kit (Cat# D3861, Thermo Scientific, USA). In brief, HuLEC-5A cells were harvested by trypsinization from 6-well plates and then resuspended in 400 μL serum-free medium containing C11-BODIPY (2 μM). Cells were incubated for 30 min at 37 °C in a cell culture incubator. Data were acquired by flow cytometers (BD Biosciences, USA) and analysed using FlowJo software.

GSH assay

Control, MFSD7C-KO and MFSD7C-Rescued HuLEC-5A cells were seeded in a 6-well plate. GSH levels were determined the next day by using the GSH reductase recycling assay (Abcam, ab239709) according to the manufacturer's instructions.

In vivo mRNA delivery and biodistribution in various organs

For in vivo codelivery of Luc mRNA and MFSD7C mRNA, mice were intravenously (i.v.) administered with Luc mRNA (0.5 mg/kg) and MFSD7C mRNA (0.5 mg/kg)–loaded hLNPs. At 6 h post-injection, mice were tail vein injected with 130 μL of 30 mg/mL D-Luciferin (PerkinElmer, MA) and imaged by using an in vivo imaging system (IVIS) (PerkinElmer, MA). To further estimate the luciferase protein expression in different organs, tissues (spleen, kidneys, liver, lungs, and heart) were isolated quickly and then imaged by the IVIS imaging system. The luminescence was quantified using Living Image software (PerkinElmer, MA).

In vitro transcription of MFSD7C mRNA

In vitro transcription of MFSD7C mRNA was prepared as described elsewhere[34]. Briefly, the Full-length mouse MFSD7C gene was cloned into In Vitro Transcription Vector for mRNA (Vector-Builder) driven by the T7 promotor. Vectors were digested using restriction endonuclease AscI (NEB, catalog no. R0558) according to the manufacturer's protocol. Capped RNA was synthesized using mMES-SAGE mMACHINE T7 Transcription Kit (Thermo Fisher Scientific, Cat# AM1344) according to the manufacturer's protocol. Synthesized RNA was purified by LiCl precipitation. RNA quality was assessed by Bioanalyzer.

Mitochondrial membrane potential assay

The mitochondrial transmembrane potential was measured by fluorescence-activated cell sorter (FACS) with the mitochondrial membrane potential assay kit (Cat# 2006, Beyotime, China) using 3′-tetraethylbenzimidazolcarbocyanine iodide (JC-1) according to the manufacturer's protocol. Cells were trypsinized and incubated with JC-1 reagent at 37 °C for 20 min, followed by flow cytometry analysis. The

ratios of red-to-green fluorescence were calculated to evaluate the mitochondrial membrane potential changes.

Intracellular ATP production assay

Intracellular ATP production was detected with Enhanced ATP Assay Kit (Cat# S2007, Beyotime, China) according to the manufacturer's protocol. Cells were trypsinized and lysed with the lysis buffer provided by the kit on ice. The supernatant of the lysate was collected and incubated with the ATP detection reagent in a 96-well plate at 37 °C for 20 min. The luminescence was detected at 560 nm by a microplate reader, and ATP production was calculated by a standard curve.

Measurement of NADP + /NADPH ratio

NADP + /NADPH ratio was measured using a NADP + /NADPH Assay Kit with WST-8 (Cat# S0179, Beyotime, China) according to the manufacturer's protocol. In brief, 1×10^6 cells were harvested and lysed by 3 frozen-thaw cycles. Cell lysate was then separated into two portions. One portion was heated at 60 °C to deplete NADP+ (only NADPH left), while the other portion was left on ice as unheated sample (containing both NADP+ and NADPH). NADP+ could be reduced into NADPH in the working buffer and the formation of NADPH further reduced WST-8 to formazan. The absorbance was then read at 450 nm with a microplate reader, and NADP + /NADPH ratio was calculated.

Untargeted lipid metabolomics analysis

Lipidomics was performed on three groups each of AMs isolated from $7C^{flox/flox}$ and $7C^{-/-}$ mice using an HPLC-MS analysis. In brief, cellular precipitate was mixed with 440 µL of H_2O and 960 µL of MTBE/MeOH (5:1; v/v). After vortexing for 60 s, the sample was sonicated 10 min and centrifuged at 660 *g* for 15 min at 4 °C, and 500 µL supernatant was collected. Then added 500 µL MTBE into the remaining solution for re-extraction. Repeated the extraction step 3 times, and combined the supernatant (1.5 mL), then evaporated to dryness at 4 °C with a vacuum concentrator. The dry extracts were then resuspended in 100 µL of DCM/MeOH (1:1; v/v). The supernatant was analyzed by HPLC–MS/MS on TripleTOF™6600 mass spectrometer (AB SCIEX, USA) coupled to an Agilent 1290 liquid chromatography system (Agilent, USA). For LC separation, Kinetex C18 column (particle size, 1.7 µm; 100 mm (length) × 2.1 mm (i.d.); Phenomenex Kinetex) was used. Mobile phase A is H_2O/ACN (6:4, v/v) with 10 mM NH_4HCOOH, mobile phase B is IPA/ACN (9:1, v/v) with 10 mM NH_4HCOOH. 2 µL sample was injected and separated with 18 min gradient. The column flow rate was maintained at 300 µL /min with the column temperature of 55 °C. Mass data were collected between m/z 200 and 2000 Da. The ion spray voltage was 5000 V for positive mode, and 4500 V for negative mode, and the heated-capillary temperature was 600 °C. LipidIMMS Analyzer was used for the list of metabolites and data matrix. Differential lipid molecules were filtered out by combining unidimensional statistical analysis and multivariate statistical analysis. Principal Component Analysis (PCA) and Partial Least Squares Discrimination Analysis (PLSDA) was performed using normalized peak table by quality control sample to investigate a possible separation of metabolite profiles between samples, and fold changes and *p* values (assessed by the student's *t* test) were computed. Criteria for differential metabolite screening: $|FC| > 1.5$, $P < 0.05$, $VIP > 1$.

LC–MS/MS analysis

Arachidonic acid level in WT and MFSD7C KO HuLEC-5A cells or lung tissues of $7C^{-/-}$ mice and HbSS mice were measured by LC-MS/MS as described previously[42,43]. Briefly, free arachidonic acid was extracted from cells or tissues using methanol, filtered through a 0.22 µm morganic membrane, and then injected into the LC-MS system for analysis. The Thermo Dionex Ultimate 3000 UHPLC system was used for chromatographic analysis. Separated them using a C18 Hypersil Gold column (3 µm, 2.1 × 100 mm, Thermo Scientific) at a flow rate of 0.3 mL/min at 35 °C. The mobile phase consisted of 0.1% (v/v) formic acid (A) and methanol (B). The gradient program was executed as follows: 0–1 min, 20% B; 1–20 min, 20–100% B; 20–27 min, 100% B; 27–28 min, 100–20% B; 28–30 min, 20% B. The injection volume was 5 µL. Performed MS on a Q-Orbitrap mass spectrometer with an ESI source. The qualitative analysis was conducted in Full MS/dd-MS2 (Top5) scan mode, scanning both positive and negative ions simultaneously. The molecular weight scan range was 100–1500. The ESI source parameters were as follows: sheath gas flow rate, 40; aux gas flow rate, 10; sweep gas flow rate, 0; spray voltage, 3.2 kV; capillary temperature, 300 °C; S-lens RF level, 50; aux gas heater temperature, 30 °C. Nitrogen was used through the entire process. The obtained data was analysed using Thermo Xcalibur Qual Browser, and the quantitative analysis was operated in negative ion full MS mode.

Metabolite uptake assay

Uptake of glucose and fatty-acid were assessed with fluorescent analogs 2-(N-(7-Nitrobenz-2-oxa-1,3-diazol-4-yl) Amino)-2-Deoxyglucose (2-NBDG, Thermo Fisher Scientific, Waltham, MA, USA, N13195) and BODIPY C16 (D3821) (Thermo Fisher Scientific, Waltham, MA, USA) using FACS as described previously[44]. Briefly, for assessment of glucose uptake, 2×10^5 WT, MFSD7C-KO and Rescued HuLEC-5A cells were incubated with glucose-free RPMI (ThermoFisher, 11879020) containing 50 µM 2-NBDG for 1 h at 37 °C. After washing with PBS + 5% FBS, the mean fluorescence intensity (MFI) of 2-NBDG in HuLEC-5A cells was analyzed by flow cytometry (BD Biosciences, USA). For assessment of fatty-acid uptake, cells were treated with 1 µM BODIPY FL-C16 and incubated for 30 min at 37 °C, then stained for flow cytometry analysis.

MitoSox assay

Mitochondrial superoxide was detected using the fluorescent MitoSox probe following the manufacturer's protocols. AMs from $7C^{-/-}$ mice and $7C^{flox/flox}$ mice, HuLEC-5A cells were incubated with 2 µM MitoSox-green (M36005, Invitrogen) for 30 min at 37 °C, washed with PBS, and the fluorescence was assessed by flow cytometry.

Statistical tests

Data are presented as mean + SD unless otherwise indicated. Two groups were compared using the two-tailed Student's *t* test. For multiple group comparisons, ANOVA with Tukey's comparisons test. Statistical analyses were performed using GraphPad Prism v.8.0 (GraphPad Software). $P < 0.05$ was considered significant.

Reporting summary

Further information on research design is available in the Nature Portfolio Reporting Summary linked to this article.

Data availability

All the data can be found in either the main text or the supplementary materials. Source data are provided with this paper. The RNA-seq data of HuLEC-5A cells generated in this study have been deposited in the NCBI GEO database under accession code GSE252686. The lipidomic data of AMs isolated from the lung of $7C^{flox/flox}$ and $7C^{-/-}$ mice generated in this study have been deposited in MetaboLights database under accession code MTBLS9293. Source data are provided with this paper.

References

1. Kato, G. J., Steinberg, M. H. & Gladwin, M. T. Intravascular hemolysis and the pathophysiology of sickle cell disease. *J. Clin. Investig.* **127**, 750–760 (2017).
2. Lamikanra, A. A. et al. Malarial anemia: of mice and men. *Blood* **110**, 18–28 (2007).

3. Hill, A. & Hill, Q. A. Autoimmune hemolytic anemia. *Hematol. Am. Soc. Hematol. Educ. Program* **2018**, 382–389 (2018).
4. Colden, M. A., Kumar, S., Munkhbileg, B. & Babushok, D. V. Insights into the emergence of paroxysmal nocturnal hemoglobinuria. *Front. Immunol.* **12**, 830172 (2021).
5. Chiabrando, D., Vinchi, F., Fiorito, V., Mercurio, S. & Tolosano, E. Heme in pathophysiology: a matter of scavenging, metabolism and trafficking across cell membranes. *Front. Pharm.* **5**, 61 (2014).
6. NaveenKumar, S. K. et al. The role of reactive oxygen species and ferroptosis in heme-mediated activation of human platelets. *ACS Chem. Biol.* **13**, 1996–2002 (2018).
7. Dixon, S. J. et al. Ferroptosis: an iron-dependent form of non-apoptotic cell death. *Cell* **149**, 1060–1072 (2012).
8. Jiang, X., Stockwell, B. R. & Conrad, M. Ferroptosis: mechanisms, biology and role in disease. *Nat. Rev. Mol. Cell Biol.* **22**, 266–282 (2021).
9. Zhou, H. et al. Ferroptosis was involved in the oleic acid-induced acute lung injury in mice. *Sheng Li Xue Bao* **71**, 689–697 (2019).
10. Yoshida, M. et al. Involvement of cigarette smoke-induced epithelial cell ferroptosis in COPD pathogenesis. *Nat. Commun.* **10**, 3145 (2019).
11. Gong, Y., Wang, N., Liu, N. & Dong, H. Lipid peroxidation and GPX4 inhibition are common causes for myofibroblast differentiation and ferroptosis. *DNA Cell Biol.* **38**, 725–733 (2019).
12. Duffy, S. P. et al. The fowler syndrome-associated protein FLVCR2 is an importer of heme. *Mol. Cell Biol.* **30**, 5318–5324 (2010).
13. Kalailingam, P. et al. Deficiency of MFSD7c results in microcephaly-associated vasculopathy in Fowler syndrome. *J. Clin. Investig.* **130**, 4081–4093 (2020).
14. Li, Y. et al. MFSD7C switches mitochondrial ATP synthesis to thermogenesis in response to heme. *Nat. Commun.* **11**, 4837 (2020).
15. Nguyen, X. T. A. et al. MFSD7c functions as a transporter of choline at the blood-brain barrier. *Cell Res.* **34**, 245–257 (2024).
16. Keleku-Lukwete, N. et al. Amelioration of inflammation and tissue damage in sickle cell model mice by Nrf2 activation. *Proc. Natl Acad. Sci. USA* **112**, 12169–12174 (2015).
17. Merle, N. S. et al. Characterization of renal injury and inflammation in an experimental model of intravascular hemolysis. *Front. Immunol.* **9**, 179 (2018).
18. Houten, S. M., Violante, S., Ventura, F. V. & Wanders, R. J. The biochemistry and physiology of mitochondrial fatty acid β-oxidation and its genetic disorders. *Annu. Rev. Physiol.* **78**, 23–44 (2016).
19. Xie, Y. et al. Ferroptosis: process and function. *Cell Death Differ.* **23**, 369–379 (2016).
20. Consoli, V. et al. Heme oxygenase modulation drives ferroptosis in TNBC Cells. *Int. J. Mol. Sci.* **23**, 5709 (2022).
21. Yamada, N. et al. Ferroptosis driven by radical oxidation of n-6 polyunsaturated fatty acids mediates acetaminophen-induced acute liver failure. *Cell Death Dis.* **11**, 144 (2020).
22. Yang, W. S. & Stockwell, B. R. Synthetic lethal screening identifies compounds activating iron-dependent, nonapoptotic cell death in oncogenic-RAS-harboring cancer cells. *Chem. Biol.* **15**, 234–245 (2008).
23. Yagoda, N. et al. RAS-RAF-MEK-dependent oxidative cell death involving voltage-dependent anion channels. *Nature* **447**, 864–868 (2007).
24. Gan, B. Mitochondrial regulation of ferroptosis. *J. Cell Biol.* **220**, e202105043 (2021).
25. Kaczmarek, J. C. et al. Optimization of a degradable polymer-lipid nanoparticle for potent systemic delivery of mRNA to the lung endothelium and immune cells. *Nano Lett.* **18**, 6449–6454 (2018).
26. Chen, J., Li, X., Ge, C., Min, J. & Wang, F. The multifaceted role of ferroptosis in liver disease. *Cell Death Differ.* **29**, 467–480 (2022).
27. Friedmann Angeli, J. P. et al. Inactivation of the ferroptosis regulator Gpx4 triggers acute renal failure in mice. *Nat. Cell Biol.* **16**, 1180–1191 (2014).
28. Bersuker, K. et al. The CoQ oxidoreductase FSP1 acts parallel to GPX4 to inhibit ferroptosis. *Nature* **575**, 688–692 (2019).
29. Devisscher, L. et al. Discovery of novel, drug-like ferroptosis inhibitors with in vivo efficacy. *J. Med. Chem.* **61**, 10126–10140 (2018).
30. Allali, S. et al. HbS promotes TLR4-mediated monocyte activation and proinflammatory cytokine production in sickle cell disease. *Blood* **140**, 1972–1982 (2022).
31. Menon, A. V. et al. Excess heme upregulates heme oxygenase 1 and promotes cardiac ferroptosis in mice with sickle cell disease. *Blood* **139**, 936–941 (2022).
32. Wang, K. et al. Locally organised and activated Fth1(hi) neutrophils aggravate inflammation of acute lung injury in an IL-10-dependent manner. *Nat. Commun.* **13**, 7703 (2022).
33. Spix, B. et al. Lung emphysema and impaired macrophage elastase clearance in mucolipin 3 deficient mice. *Nat. Commun.* **13**, 318 (2022).
34. Qiu, M. et al. Lung-selective mRNA delivery of synthetic lipid nanoparticles for the treatment of pulmonary lymphangioleiomyomatosis. *Proc. Natl Acad. Sci. USA* **119**, e2116271119 (2022).
35. Daly, T. A., Almeida, P. F. & Regen, S. L. Sorting of lipidated peptides in fluid bilayers: a molecular-level investigation. *J. Am. Chem. Soc.* **134**, 17245–17252 (2012).
36. Tseng, Y. J. et al. Increased iron uptake by splenic hematopoietic stem cells promotes TET2-dependent erythroid regeneration. *Nat. Commun.* **15**, 538 (2024).
37. D'Alessandro-Gabazza, C. N. et al. Inhibition of lung microbiota-derived proapoptotic peptides ameliorates acute exacerbation of pulmonary fibrosis. *Nat. Commun.* **13**, 1558 (2022).
38. Duerr, J. et al. Conditional deletion of Nedd4-2 in lung epithelial cells causes progressive pulmonary fibrosis in adult mice. *Nat. Commun.* **11**, 2012 (2020).
39. Gibson-Corley, K. N., Olivier, A. K. & Meyerholz, D. K. Principles for valid histopathologic scoring in research. *Vet. Pathol.* **50**, 1007–1015 (2013).
40. Huebner, R.-H. et al. Standardized quantification of pulmonary fibrosis in histological samples. *Biotechniques* **44**, 507 (2008). +.
41. McQualter, J. L. et al. Endogenous fibroblastic progenitor cells in the adult mouse lung are highly enriched in the Sca-1 positive cell fraction. *Stem Cells* **27**, 623–633 (2009).
42. Zhang, J. Z. et al. Spatial distribution, antioxidant capacity, and spore germination-promoting effect of Bibenzyls from. *Antioxidants* **11**, 2157 (2022).
43. Xiong, R. L. et al. Identification and characterization of two bibenzyl glycosyltransferases from the liverwort. *Antioxidants* **11**, 735 (2022).
44. Waickman, A. T. et al. Dissecting the heterogeneity of DENV vaccine-elicited cellular immunity using single-cell RNA sequencing and metabolic profiling. *Nat. Commun.* **10**, 3666 (2019).

Acknowledgements

This work was supported by National Key R&D Program of China (No. 2023YFC3404100), National Natural Science Foundation of China Grant (No. 82373784), Excellent Young Scholars of Shandong Province of China (No. 2022HWYQ-033, 2022HWYQ-029), and Young Scholars of Taishan (tsqn202211035), National Natural Science Foundation of China (Nos. 82204404, 82293682, 82173703, 82100185). We thank Translational Medicine Core Facility of Shandong University for consultation and instrument availability that supported this work. The Figs. 3a, 6j, 7d and Supplementary Fig. 1a partly generated using Servier Medical Art, provided by Servier, licensed under a Creative Commons Attribution 3.0 unported license.

Author contributions

H.W. and X.Y.: experimental design/or execution, data analyzing, as well as writing/or reviewing manuscript; J.W.: compounds synthesis in this paper; X.C.: data analyzing and writing manuscript; Y.G., M.W., W.Z., Y.Y., B.H., M.Q., and J.Z.: conducted experiments and analyzed data; X.L., H.L., and T.D.: study supervision, experimental design and reviewing manuscript.

Competing interests

The authors declare no competing interests.

Additional information

Supplementary information The online version contains supplementary material available at https://doi.org/10.1038/s41467-024-52537-6.

Correspondence and requests for materials should be addressed to Xiaohui Liu, Hongxiang Lou or Ting Dong.

Peer review information *Nature Communications* thanks Dar-Bin Shieh and Alan Brash, and the other, anonymous, reviewer(s) for their contribution to the peer review of this work. A peer review file is available.